

DIAGNOSTIC ANALYSIS OF HEAVY RAINFALL EVENTS OVER THE YANGTZE
RIVER VALLEY DURING THE MEI-YU SEASON 2020

A THESIS SUBMITTED TO THE GRADUATE DIVISION OF THE
UNIVERSITY OF HAWAII IN PARTIAL FULFILLMENT OF THE
REQUIREMENTS FOR THE DEGREE OF
MASTER OF SCIENCE
IN
ATMOSPHERIC SCIENCES

DECEMBER 2020

By
Qi-Zhen Sun

Thesis Committee:

Yi-Leng Chen, Chairperson

Tim Li

Torri Giuseppe

Abstract

During the early summer rainy season of the southern China plain in 2020, series of unprecedented heavy Mei-Yu precipitation occurred over the Yangtze River Valley region accompanied by a widespread inundation. Compared with the past ten-year mean conditions (2011-2019), the Mei-Yu precipitation over the Yangtze River Valley in 2020 shows that there was an occurrence of downpour over a longer lasting period (62 days in total). By using the CFSv2 reanalysis data with 6-hourly interval (2011-2020), a low-level boundary layer jet over the north part of South China Sea is diagnosed and referred to as Marine Boundary Layer Jet (MBLJ) by previous studies (Chen et al. 2018, Tu et al. 2019). This boundary layer jet has shown its wind maximum around 925-hPa with relatively large horizontal moisture transport is confined to the boundary layer for almost the entire Mei-Yu season (from June 1st to July 31st) in 2020. The MBLJ is mainly related to the large sub-synoptic scale pressure gradients between a stronger than normal WPSH and a South-West Vortex (SWV) originating from the lee side of the Tibet Plateau (Tu et al. 2019, Tu et al. 2020). Accompanied with a relatively stronger low-level wind ($> 10 \text{ ms}^{-1}$) within the MBL During the Mei-Yu season in 2020, the MBLJ over the Northern South China Sea played a key role in transporting the low-level moisture from the subtropical ocean to the southern China plain, contributing to the heavy precipitation over the Yangtze River valley that lasted almost for the entire rainy season. In addition to the S-N moisture supply by the MBLJ, a southwesterly sub-synoptic Low-Level (SLLJ) along the Mei-Yu front was (Chen and Yu 1988) present as a result of the secondary circulation associated with the Mei-Yu frontal circulation (Chen et al., 1994). During the Mei-Yu season in 2020, the MBLJ encountered the SLLJ along with the Mei-Yu front after reaching the southern China plain. The MBLJ brings in excessive moisture from the northern South China Sea to the central China plain where the rainfall production is mainly related to the secondary circulation associated with the Mei-Yu jet/front system. Moreover, the moisture transport is dominated by the mean flow with much less contribution in the transient mode. With this favorable synergistic effect caused by both MBLJ and SLLJ together, series of unprecedented long-lasting rainfall events occurred over the Yangtze River Valley during the entire 2020 Mei-Yu season.

List of Contents

Abstract	ii
List of Figures	iv
1. Introduction	1
2. Data and Methodology	5
3. Results	7
3.1 Rainfall Distributions	7
3.2 Synoptic Overview	9
3.3 The WPSH Anomalies	18
3.4 Moisture Transportation During the Mei-Yu Season 2020	20
3.5 The Synergistic Effect of SLLJ and MBLJ	32
4. Summary	46
APPENDIX	49
References	57

List of Figures

Figure 1. Average Daily Precipitation Rate Anomalies (mm/day) between 2020 and 2011-2019 ten-year mean conditions. (a) June 1 – June 15. (b) June 16 – June 30. (c) July 1 – July 15. (d) July 16 – July 31. 8

Figure 2. June 1 – June 15 CFSR 15-Days Average (a) composite map of the 925-hPa winds (m/s), geopotential height (gpm) and equivalent potential temperature (K) for the 2011-2019 ten-year mean conditions. (b) As in (a) but for the 2020. (c) Difference in wind (m/s), geopotential height (gpm) and equivalent potential temperature (K) between 2020 and 2011-2019 long term mean conditions. 9

Figure 3. June 16 – June 30 CFSR 15-Days Average (a) composite map of the 925-hPa winds (m/s), geopotential height (gpm) and equivalent potential temperature (K) for the 2011-2019 ten-year mean conditions. (b) As in (a) but for the 2020. (c) Difference in wind (m/s), geopotential height (gpm) and equivalent potential temperature (K) between 2020 and 2011-2019 long term mean conditions. 10

Figure 4. July 1 – July 15 CFSR 15-Days Average (a) composite map of the 925-hPa winds (m/s), geopotential height (gpm) and equivalent potential temperature (K) for the 2011-2019 ten-year mean conditions. (b) As in (a) but for the 2020. (c) Difference in wind (m/s), geopotential height (gpm) and equivalent potential temperature (K) between 2020 and 2011-2019 long term mean conditions. 11

Figure 5. July 16 - July 31 CFSR 15-Days Average (a) composite map of the 925-hPa winds (m/s), geopotential height (gpm) and equivalent potential temperature (K) for the 2011-2019 ten-year mean conditions. (b) As in (a) but for the 2020. (c) Difference in wind (m/s), geopotential height (gpm) and equivalent potential temperature (K) between 2020 and 2011-2019 long term mean conditions. 13

Figure 6. CFSR 15-Days Average (a) June 1 – June 15 composite map of 925-hPa winds anomalies (m/s), geopotential height anomalies (gpm), potential temperature anomalies (K) between 2011-2019 ten-year mean conditions and 2020. (b) As in (a) but for June 16 – June 30. (c) As in (a) but for July 1 – July 15. (d) As in (a) but for July 16 – July 31. 14

Figure 7. 15-days Average CFSR composite map of 500-hPa winds anomalies (m/s), geopotential height anomalies (gpm) and vertical pressure velocity anomalies (pa/s) for (a) June 1 – June 15. (b) June 16 – June 30. (c) July 1 – July 15. (d) July 16 – July 31. 16

Figure 8. MJO Phase Evaluation during the Mei-Yu season 2020 obtained from the MJO Report prepared by the Climate Prediction Center (NCEP); The yellow line represents an ensemble member; the bold green line represents the ensemble mean and the light (dark) gray shading represents the area in which 50% (90%) of the ensemble members reside. (a) May 31 – June 14. (b) June 15 – June 29. (c) July 5 – July 19. (d) July 13 – July 27. 19

Figure 9. June 1 – 15 Average CFSR (a) composite map of the 925-hPa winds (m/s), geopotential height (gpm) and TPW (mm) for the 2011-2019 ten-year mean conditions. (b) As in (a) but for the 2020. (c) Difference in wind (m/s), geopotential height (gpm) and TPW (mm) for the 2011-2019 ten-year mean conditions. 20

Figure 10. June 16-30 Average CFSR (a) composite map of the 925-hPa winds (m/s), geopotential height (gpm) and TPW (mm) for the 2011-2019 ten-year mean conditions. (b) As in (a) but for the 2020. (c) Difference in wind (m/s), geopotential height (gpm) and TPW (mm) between 2020 and 2011-2019 long term mean conditions. 21

Figure 11. July 1-15 Average CFSR (a) composite map of the 925-hPa winds (m/s), geopotential height (gpm) and TPW (mm) for the 2011-2019 ten-year mean conditions. (b) As in (a) but for the 2020. (c) Difference in wind (m/s), geopotential height (gpm) and TPW (mm) between 2020 and 2011-2019 long term mean conditions.	22
Figure 12. July 16-31 Average CFSR (a) composite map of the 925-hPa winds (m/s), geopotential height (gpm) and TPW (mm) for the 2011-2019 ten-year mean conditions. (b) As in (a) but for the 2020. (c) Difference in wind (m/s), geopotential height (gpm) and TPW (mm) between 2020 and 2011-2019 long term mean conditions.	23
Figure 13. CFSR 15-Days Average (a) June 1 – June 15 composite map of 850-hPa winds anomalies (m/s), geopotential height anomalies (gpm), equivalent potential temperature anomalies (K) between 2011-2019 ten-year mean conditions and 2020. (b) As in (a) but for June 16 – June 30. (c) As in (a) but for July 1 – July 15. (d) As in (a) but for July 16 – July 31.	24
Figure 14. CFSR 15-Days Average (a) June 1 – June 15 composite map of 925-hPa “Q-flux” anomalies ($\text{g} \cdot \text{kg}^{-1} \cdot \text{m} \cdot \text{s}^{-1}$) between 2011-2019 ten-year mean conditions and 2020. (b) As in (a) but for June 16 – June 30. (c) As in (a) but for July 1 – July 15. (d) As in (a) but for July 16 – July 31.	25
Figure 15. CFSR 15-Days Average (a) June 1 – June 15 composite map of 850-hPa “Q-flux” anomalies ($\text{g} \cdot \text{kg}^{-1} \cdot \text{m} \cdot \text{s}^{-1}$) between 2011-2019 ten-year mean conditions and 2020. (b) As in (a) but for June 16 – June 30. (c) As in (a) but for July 1 – July 15. (d) As in (a) but for July 16 – July 31.	26
Figure 16. June 1-15 CFSR 15-days Average (a) IVT ($\text{kg} \cdot \text{m}^{-1} \cdot \text{s}^{-1}$) within the boundary layer (below 900-hPa) for 2011-2019 ten-year mean conditions. (b) As in (a) but for the 2020. (c) Difference in IVT ($\text{kg} \cdot \text{m}^{-1} \cdot \text{s}^{-1}$) between 2020 and 2011-2019 long term mean conditions.	27
Figure 17. June 16-30 CFSR 15-days Average (a) IVT ($\text{kg} \cdot \text{m}^{-1} \cdot \text{s}^{-1}$) within the boundary layer (below 900-hPa) for 2011-2019 ten-year mean conditions. (b) As in (a) but for the 2020. (c) Difference in IVT ($\text{kg} \cdot \text{m}^{-1} \cdot \text{s}^{-1}$) between 2020 and 2011-2019 long term mean conditions.	28
Figure 18. July 1-15 CFSR 15-days Average (a) IVT ($\text{kg} \cdot \text{m}^{-1} \cdot \text{s}^{-1}$) within the boundary layer (below 900-hPa) for 2011-2019 ten-year mean conditions. (b) As in (a) but for the 2020. (c) Difference in IVT ($\text{kg} \cdot \text{m}^{-1} \cdot \text{s}^{-1}$) between 2020 and 2011-2019 long term mean conditions.	29
Figure 19. July 16-31 CFSR 15-days Average (a) IVT ($\text{kg} \cdot \text{m}^{-1} \cdot \text{s}^{-1}$) within the boundary layer (below 900-hPa) for 2011-2019 ten-year mean conditions. (b) As in (a) but for the 2020. (c) Difference in IVT ($\text{kg} \cdot \text{m}^{-1} \cdot \text{s}^{-1}$) between 2020 and 2011-2019 long term mean conditions.	30
Figure 20. 2020 CFSR 15-days Average Transient IVT ($\text{kg} \cdot \text{m}^{-1} \cdot \text{s}^{-1}$) within the boundary layer (below 900-hPa) (a) June 1 – June 15. (b) June 16 – June 30. (c) July 1 – July 15. (d) July 16 – July 31.	31
Figure 21. The position of tilting Cross-section axis (Black Solid Line) along ($18^{\circ}\text{N}, 118^{\circ}\text{E} - 32^{\circ}\text{N}, 104^{\circ}\text{E}$) and meridional cross-section axis (Red Solid Line) along ($17^{\circ}\text{N}, 115^{\circ}\text{E} - 34^{\circ}\text{N}, 115^{\circ}\text{E}$). The shading area indicates terrain height (m). The black solid line shows the location of cross-sections displayed in this section and the red solid line indicates the location of meridional cross-sections displayed in the Appendix.	32
Figure 22. June 1-June 15. CFSR 15-days average cross-sections along ($18^{\circ}\text{N}, 118^{\circ}\text{E} - 32^{\circ}\text{N}, 104^{\circ}\text{E}$) for 2011-2019 ten-year mean. (a) Composite map of horizontal winds (m/s) and potential temperature (K). (b) Composite map of horizontal wind and specific humidity (g/kg). (c) Horizontal moisture flux ($\text{g} \cdot \text{kg}^{-1} \cdot \text{m} \cdot \text{s}^{-1}$). (d) Composite map of vertical velocity (pa/s) and equivalent potential temperature (K). (e) Composite map of atmospheric circulation and equivalent potential temperature (K). The grey shading area indicates terrain.	34

Figure 23. June 16-June 30. CFSR 15-days average cross-sections along ($18^{\circ}N, 118^{\circ}E - 32^{\circ}N, 104^{\circ}E$) for 2011-2019 ten-year mean. (a) Composite map of horizontal winds (m/s) and potential temperature (K). (b) Composite map of horizontal wind and specific humidity (g/kg). (c) Horizontal moisture flux ($g \cdot kg^{-1} \cdot m \cdot s^{-1}$). (d) Composite map of vertical velocity (pa/s) and equivalent potential temperature (K). (e) Composite map of atmospheric circulation and equivalent potential temperature (K). The grey shading area indicates terrain. 35

Figure 24. July 1-July 15. CFSR 15-days average cross-sections along ($18^{\circ}N, 118^{\circ}E - 32^{\circ}N, 104^{\circ}E$) for 2011-2019 ten-year mean. (a) Composite map of horizontal winds (m/s) and potential temperature (K). (b) Composite map of horizontal wind and specific humidity (g/kg). (c) Horizontal moisture flux ($g \cdot kg^{-1} \cdot m \cdot s^{-1}$). (d) Composite map of vertical velocity (pa/s) and equivalent potential temperature (K). (e) Composite map of atmospheric circulation and equivalent potential temperature (K). The grey shading area indicates terrain. 36

Figure 25. July 16-July 31. CFSR 15-days average cross-sections along ($18^{\circ}N, 118^{\circ}E - 32^{\circ}N, 104^{\circ}E$) for 2011-2019 ten-year mean. (a) Composite map of horizontal winds (m/s) and potential temperature (K). (b) Composite map of horizontal wind and specific humidity (g/kg). (c) Horizontal moisture flux ($g \cdot kg^{-1} \cdot m \cdot s^{-1}$). (d) Composite map of vertical velocity (pa/s) and equivalent potential temperature (K). (e) Composite map of atmospheric circulation and equivalent potential temperature (K). The grey shading area indicates terrain. 37

Figure 26. June 1-June 15. CFSR 15-days average cross-sections along ($18^{\circ}N, 118^{\circ}E - 32^{\circ}N, 104^{\circ}E$) for 2020. (a) Composite map of horizontal winds (m/s) and potential temperature (K). (b) Composite map of horizontal wind and specific humidity (g/kg). (c) Horizontal moisture flux ($g \cdot kg^{-1} \cdot m \cdot s^{-1}$). (d) Composite map of vertical velocity (pa/s) and equivalent potential temperature (K). (e) Composite map of atmospheric circulation and equivalent potential temperature (K). The grey shading area indicates terrain. 38

Figure 27. June 16-June 30. CFSR 15-days average cross-sections along ($18^{\circ}N, 118^{\circ}E - 32^{\circ}N, 104^{\circ}E$) for 2020. (a) Composite map of horizontal winds (m/s) and potential temperature (K). (b) Composite map of horizontal wind and specific humidity (g/kg). (c) Horizontal moisture flux ($g \cdot kg^{-1} \cdot m \cdot s^{-1}$). (d) Composite map of vertical velocity (pa/s) and equivalent potential temperature (K). (e) Composite map of atmospheric circulation and equivalent potential temperature (K). The grey shading area indicates terrain. 39

Figure 28. July 1-July 15. CFSR 15-days average cross-sections along ($18^{\circ}N, 118^{\circ}E - 32^{\circ}N, 104^{\circ}E$) for 2020. (a) Composite map of horizontal winds (m/s) and potential temperature (K). (b) Composite map of horizontal wind and specific humidity (g/kg). (c) Horizontal moisture flux ($g \cdot kg^{-1} \cdot m \cdot s^{-1}$). (d) Composite map of vertical velocity (pa/s) and equivalent potential temperature (K). (e) Composite map of atmospheric circulation and equivalent potential temperature (K). The grey shading area indicates terrain. 40

Figure 29. July 16-July 31. CFSR 15-days average cross-sections along ($18^{\circ}N, 118^{\circ}E - 32^{\circ}N, 104^{\circ}E$) for 2020. (a) Composite map of horizontal winds (m/s) and potential temperature (K). (b) Composite map of horizontal wind and specific humidity (g/kg). (c) Horizontal moisture flux ($g \cdot kg^{-1} \cdot m \cdot s^{-1}$). (d) Composite map of vertical velocity (pa/s) and equivalent potential temperature (K). (e) Composite map of atmospheric circulation and equivalent potential temperature (K). The grey shading area indicates terrain. 41

Figure 30. June 15 – July 31, 2020 CFSR average composite meridional cross-section along ($18^{\circ}N, 118^{\circ}E - 32^{\circ}N, 104^{\circ}E$) (a) The tendency term ($(\partial \bar{q}) / \partial t$) ($10^{-5} g \cdot kg^{-1} \cdot s^{-1}$). (b) The horizontal Advection Term ($-V \cdot \nabla \bar{q}$) ($10^{-5} g \cdot kg^{-1} \cdot s^{-1}$). (c) The Vertical Advection Term

$(-\omega\partial q\partial p)$ ($10^{-5}\text{g} \cdot \text{kg}^{-1} \cdot \text{s}^{-1}$). (d) Subgrid-scale Term $(-c - e + \partial q' \omega'/\partial p)$ ($10^{-5}\text{g} \cdot \text{kg}^{-1} \cdot \text{s}^{-1}$).
The grey shading area indicates terrain. 44

Figure 31. 2020 15-days Average Daily Precipitation Rate (mm/day) Rebuild
Distribution (a)June 1 – June 15. (b)June 16 – June 30 (c)July 1– July 15. (d)July 16 – July 31.
..... 45

Figure 32. As in Fig.22 but for meridional cross-section along $(18^\circ\text{N}, 118^\circ\text{E} - 32^\circ\text{N}, 104^\circ\text{E})$ 49

Figure 33. As in Fig.23 but for meridional cross-section along $(18^\circ\text{N}, 118^\circ\text{E} - 32^\circ\text{N}, 104^\circ\text{E})$ 50

Figure 34. As in Fig.24 but for meridional cross-section along $(18^\circ\text{N}, 118^\circ\text{E} - 32^\circ\text{N}, 104^\circ\text{E})$ 51

Figure 35. As in Fig.25 but for meridional cross-section along $(18^\circ\text{N}, 118^\circ\text{E} - 32^\circ\text{N}, 104^\circ\text{E})$ 52

Figure 36. As in Fig.26 but for meridional cross-section along $(18^\circ\text{N}, 118^\circ\text{E} - 32^\circ\text{N}, 104^\circ\text{E})$ 53

Figure 37. As in Fig.27 but for meridional cross-section along $(18^\circ\text{N}, 118^\circ\text{E} - 32^\circ\text{N}, 104^\circ\text{E})$ 54

Figure 38. As in Fig.28 but for meridional cross-section along $(18^\circ\text{N}, 118^\circ\text{E} - 32^\circ\text{N}, 104^\circ\text{E})$ 55

Figure 39. As in Fig.22 but for meridional cross-section along $(18^\circ\text{N}, 118^\circ\text{E} - 32^\circ\text{N}, 104^\circ\text{E})$ 56

1. Introduction

During the early summer rainy seasons over the East Asia, one of the most significant and unique weather phenomena is the Mei-Yu (“Baiu”) precipitation with frequent heavy rainfall occurrences (> 100 mm per daily) (Chen and Yu 1988). The Mei-Yu precipitation shows its main impact regions in the middle and lower reaches of the Yangtze River Valley in China, Taiwan, South Central Japan, and South Korea in late spring and early summer season but with a slight difference depending on its location. Based on the characteristics of Mei-Yu rainband migration, every year the Mei-Yu precipitation first appears in the Taiwan area (early May) when the moist summertime monsoon flow confronted with the cool polar air masses from the East Asia continent. After that, the strong thermal and moist contrast weather pattern caused by the two different air masses will migrate to the southern China plain and linger around that place when the Mei-Yu precipitation finally affects the Yangtze River Valley in mid and late June. With some mesoscale weather systems and the local terrain effects, the long-lasting rainfall occurrences over the East Asia during the early summer rainy season may produce strong flooding, landslides, reservoir bursts, property loss and casualties.

Recent studies (Chen and Yu 1988, Chen et al. 1995, Tu et al. 2019, Tu et al. 2020) show that the occurrence of Mei-Yu precipitation is usually accompanied with a synoptic low-level front which usually possesses a nearly continuous cloud band with local strong convection along the front. This Mei-Yu front usually forms between the cool polar air and warm subtropical air masses with a relatively larger thermal gradients and moist contrast, lingering around the southern China plain and Yangtze River Valley from mid and late June to mid-July.

From the observations and analysis of modeling data, there are several synoptic characteristics during the Mei-Yu rainy season over the East Asia, including a high-pressure cell at the 500-hPa level moving from the south Asia to between 20°N and 25°N as the season progresses (Chen 1993) with westerly circulation occurred over north of the Tibetan Plateau and frequent shortwave activities which provide cold air masses invading into the southern China plain.

The Western Pacific Subtropical High (WPSH) has an obvious westward extension and northward jump during this Mei-Yu rainy season. Before the Mei-Yu precipitation began to affect the Yangtze River Basin (May and early June), the ridgeline of WPSH has been located at lower latitude (south of 20°N) with the warm and moist southwesterly flow along the southwestern periphery intersecting frequent colder polar air mass intruding from higher latitudes behind a mid-latitude shortwave trough to the southern China plain. During the regular Mei-Yu season over Yangtze River Valley starting from mid and late June, the ridgeline of the WPSH at 925-hPa is between 20°N and 25°N, with the warm and moist southwesterly monsoon flow prevailing along the southwesterly edge of the subtropical high to the Yangtze River Basin (Chen 1989, Chen 1993). Under these circulation patterns, the Mei-Yu front lingers in the Yangtze River Basin, often accompanied by Southwest Vortex (SWV) and a sub-synoptic southwesterly Low-level Jet (SLLJ) (Chen and Yu 1988) to the south of the Mei-Yu front in the 850-750 layers. The existence of SWV and the SLLJ south of the Mei-Yu front is considered as an important factor in maintaining the heavy precipitation in the Mei-Yu season and providing abundant moisture supply for the rainstorm (Chen and Zhang 1994, Chen and Chen 1995, Chen and Yu 1988). The development of the LLJ along the Mei-Yu front is largely a mass-momentum adjustment process in response to moist baroclinic forcing which is associated with the secondary circulation of the jet front system (Chen et al, 1994, 1997, Chen and Chen 1995).

During the 2020 Mei-Yu season, series of significant flood events occurred over the central and eastern China plain (Yangtze River Valley) due to the occurrences of extremely Mei-Yu precipitation (Fig. 1). During June to July 2020, the average precipitation in southern China was 436 mm, 18% more than the ten-year mean conditions in the same period of the year and is the second largest in the same period since 1961. More than 10 million people in Guangxi, Guizhou, Hunan, Sichuan, Jiangxi, and other provinces were affected by floods caused by the rainfall in the southern plain and the Yangtze River Valley. Compared with the previous ten-year mean conditions of traditional Mei-Yu precipitation, the Mei-Yu precipitation occurred over the Yangtze River Valley this year started earlier than usual and ended late, lasting for 62 days in total, which has been the longest Mei-Yu case since 1961. The amount of precipitation reached 759.2 mm, which is also the highest level since 1961. These unusual Mei-Yu precipitation events with the

significant flooding caused tremendous disasters and deplorable economic losses during the 2020 Mei-Yu (Fig. 1).

Usually, during the early summer rainy season of East Asia, the low-level southwesterly monsoon flow prevails over the northern South China Sea. According to recent studies by [Chen et al. \(2018\)](#), [Tu et al. \(2019\)](#) and [Tu et al. \(2020\)](#), during the early summer rainy season of Taiwan area, a strong low-level wind maximum core with large horizontal moisture transport within the boundary layer (below 900-hPa) can be found over the South China Sea which is frequently accompanied by heavy precipitation occurrences over the Taiwan area. This strong low-level boundary jet over the northern South China Sea, is referred to as “the Marine Boundary Layer Jet” (MBLJ) by these studies ([Chen et al. 2018](#), [Tu et al. 2019](#), [Tu et al. 2020](#)). The strong low-level southwesterly flow is related to the large pressure gradients between the SWV and the WPSH. It has a strong low-level wind maximum ($> 10 \text{ ms}^{-1}$) (around 950-hPa) with large horizontal moisture fluxes ($> 160 \text{ g} \cdot \text{kg}^{-1} \cdot \text{ms}^{-1}$) from the northern South China Sea to Taiwan. The existence of MBLJ has been overlooked in many heavy rainfall studies and in real-time operational forecasts.

The main purpose of this article is to establish the potential relationship between the existence of marine boundary layer jet over the northern South China Sea and the unusually heavy precipitation and the significant flooding events that occurred over the Yangtze River Valley during the 2020 Mei-Yu season. I will focus on the reasons why the heavy rainfall events over the Yangtze River Valley during the 2020 Mei-Yu were so frequent, it started early and lasted longer when compared with the common Mei-Yu case during the past decade. I want to explain more clearly the causes of abnormal precipitation occurred over the Yangtze River Basin in 2020 and its possible link to the MBLJ. When compared with the ten-year mean conditions (2011-2019), the synoptic weather pattern differences and abnormal moisture transport will be discussed in this study. We will investigate the possible synergistic effects caused by SLLJ which is related to the secondary circulation of the Mei-Yu front ([Chen et al., 1994; 1997](#)) and MBLJ over the northern South China Sea. I will investigate the meteorological characteristics of, synoptic circulation patterns, thermodynamic differences and the related moisture budget balance. The possible factors

that may determine the locations and occurrences of the MBLJ in relationship to the variations in WPSH and the SWV will also be deal with.

2. Data and Methodology

The synoptic reanalysis data used in this diagnostic study were obtained from the NCEP Climate Forecast System Version 2 (CFSv2) 6-hourly Products with $0.5^\circ \times 0.5^\circ$ horizontal resolution. The meteorological elements involved are precipitable water, precipitation rate, temperature, specific humidity, potential temperature, geopotential height, horizontal velocity in meridional and zonal direction, and vertical pressure velocity. A basic review and description of various criteria for identifying MBLJ in the previous study is given by [Tu et al. \(2019\)](#).

By using the diagnostic method in synoptic meteorology, we use Integrated Vapor Transport (IVT) to illustrate the horizontal moisture transport within the troposphere which is largely associated with the MBLJ during the 2020 Mei-Yu season. The zonal and meridional component of the integrated vapor transport (IVT) within a specific atmospheric layer is given as followed:

$$Q_\lambda = \frac{1}{g} \int_{p_s}^{p_t} u \cdot q \, dp \quad (1)$$

$$Q_\phi = \frac{1}{g} \int_{p_s}^{p_t} v \cdot q \, dp \quad (2)$$

Where g is the gravity acceleration, p_t is the atmospheric pressure at the top of the layer, p_s is the ground pressure value, u is the zonal wind, v is the meridional wind and q is the specific humidity. Considering that the water vapor content above 300hPa is very small in the atmosphere, the 300-hPa level is used as the upper limit for vertical integration.

We also use moist budget equation ([Yanai et al. 1973](#)) to further discuss the moisture balance over the Mei-Yu frontal area:

$$\frac{\partial \bar{q}}{\partial t} = -\bar{V} \cdot \nabla \bar{q} - \bar{\omega} \frac{\partial \bar{q}}{\partial p} - [(\bar{c} - \bar{e}) + (\overline{\partial q' \omega'} / \partial p)] \quad (3)$$

where q is the specific humidity, t is time, V is the horizontal velocity, ∇ is the gradient operator, p is the pressure, ω is the vertical pressure velocity, c is the rate of condensation per unit mass of air, and e is the rate of evaporation.

$$\mathbf{R} = - \int_{P_B}^{P_T} (\bar{c} - \bar{e}) \frac{dp}{g} \quad (4)$$

The net Rainfall per unit time (\mathbf{R}) (Ogura and Cho, 1973) was also used to diagnose the net precipitation rate from the moisture budget:

$$\therefore \frac{\partial \bar{q}}{\partial t} + \bar{V} \cdot \nabla \bar{q} + \bar{\omega} \frac{\partial \bar{q}}{\partial p} = -[(\bar{c} - \bar{e}) + (\partial \overline{q' \omega'} / \partial p)] \quad (5)$$

$$\therefore \int_{P_B}^{P_T} \left[\frac{\partial \bar{q}}{\partial t} + \bar{V} \cdot \nabla \bar{q} + \bar{\omega} \frac{\partial \bar{q}}{\partial p} \right] \frac{dp}{g} = - \int_{P_B}^{P_T} (\bar{c} - \bar{e}) \frac{dp}{g} - \int_{P_B}^{P_T} (\partial \overline{q' \omega'} / \partial p) \frac{dp}{g} \quad (6)$$

\mathbf{A} \mathbf{B} \mathbf{C}

Where P_T is the pressure at the top of the troposphere, P_B is the surface pressure. Term \mathbf{A} can be calculated from the moist budget equation which consists of the tendency term, horizontal convection term and vertical convection term. Term \mathbf{C} is the vertical integral of the eddy moisture fluxes which equals the surface evaporation. The vertical integral of net precipitations (Term \mathbf{B}) in the moist budget equation equals \mathbf{R} .

3. Results

3.1 Rainfall Distributions

The total Mei-Yu precipitation patterns during the summer rainy season 2020 over the Yangtze River Valley has shown extraordinary heavy rainfall when compared with ten-year mean (2010-2019) during the same time period (Fig. 1), In order to better depict the evolution of variations over the flooding region during the 2020 Mei-Yu season, every month within this period has been divided into two parts (15 days average) and compared to the ten-year (2011-2019) mean to help us better understand the bi-monthly variations of anomalies during this time period.

The precipitation anomalies of the 2020 Mei-Yu season (1 June – 31 July) (Fig. 1) show that its maximum around the central and eastern parts of the China plain (Yangtze River Valley) which corresponds well with the flooding areas such as Qijiang, Enshi, Huangshan.... On the other hand, the Taiwan and the southern China coastal areas had relatively less rainfall when compared to the ten-year mean, since it is under the WPSH influence with suppression conditions. The rainfall maximum region with southwest to northeast tilting belt is extended from the southern China plain to further area such as Japan and Korea, indicating that those places are subject to the impact of heavy Mei-Yu precipitation during the early summer rainy season 2020 as well.

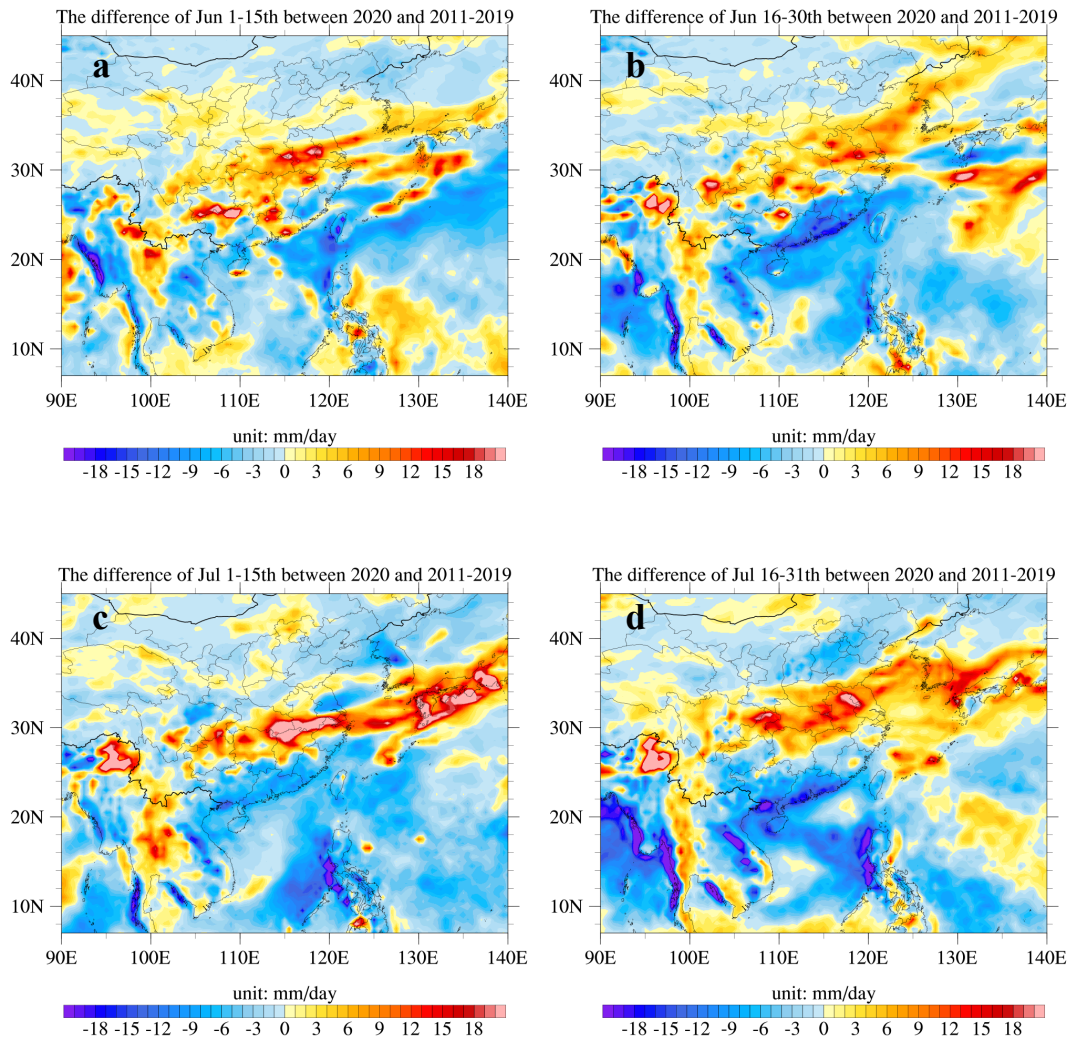


Figure 1. Average Daily Precipitation Rate Anomalies (mm/day) between 2020 and 2011-2019 ten-year mean conditions. (a) June 1 – June 15. (b) June 16 – June 30. (c) July 1 – July 15. (d) July 16 – July 31.

3.2 Synoptic Overview

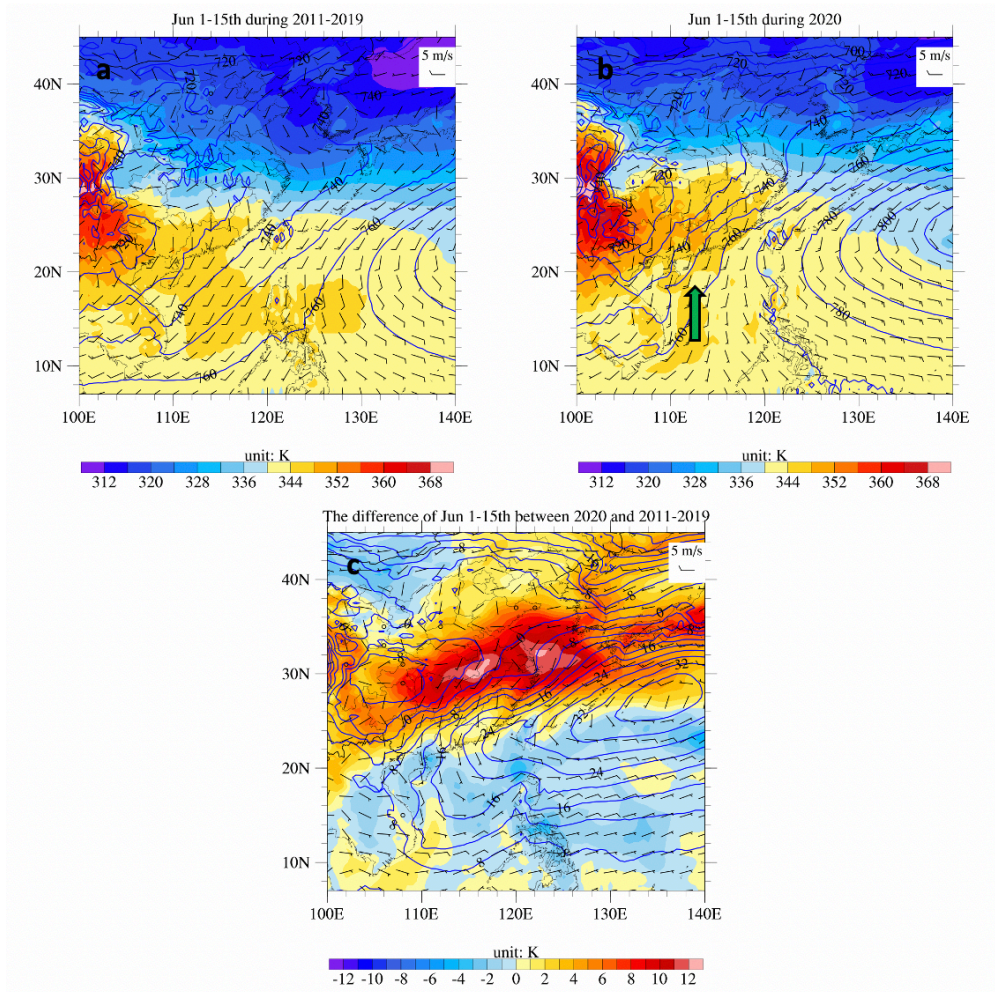


Figure 2. June 1 – June 15 CFSR 15-Days Average (a) composite map of the 925-hPa winds (m/s), geopotential height (gpm) and equivalent potential temperature (K) for the 2011-2019 ten-year mean conditions. (b) As in (a) but for the 2020. (c) Difference in wind (m/s), geopotential height (gpm) and equivalent potential temperature (K) between 2020 and 2011-2019 long term mean conditions.

During the Mei-Yu season, the WPSH always plays an important role in the controlling of East Asia weather patterns with greater strength and wider scope of influence area. The northward migration of the ridge axis of WPSH to around 20°N usually occurs at the beginning of the Mei-Yu precipitation over the Yangtze River Valley (Fig. 2a and 3a). The southwesterly summer monsoon flow along the southwestern Periphery of WPSH gathers strength during the southeastward advance of a midlatitude shortwave trough from the north. A continuous large-scale convective cloud band occurs where the intruding cold air converges with the southeasterly flow

in the Yangtze River Valley. In the meantime, a low-pressure system (South-West Vortex) frequently forms in the leeside of the Tibetan Plateau or the Yun-Guei Plateau and travels eastward along with the Mei-Yu front zone (Chen and Yu, 1988). It is worth pointing out that even though the previous Mei-Yu precipitation occurrence over the Yangtze River Valley displays long-lasting characteristics, it may not cause so much heavy flooding events as what occurred in the 2020 Mei-Yu season.

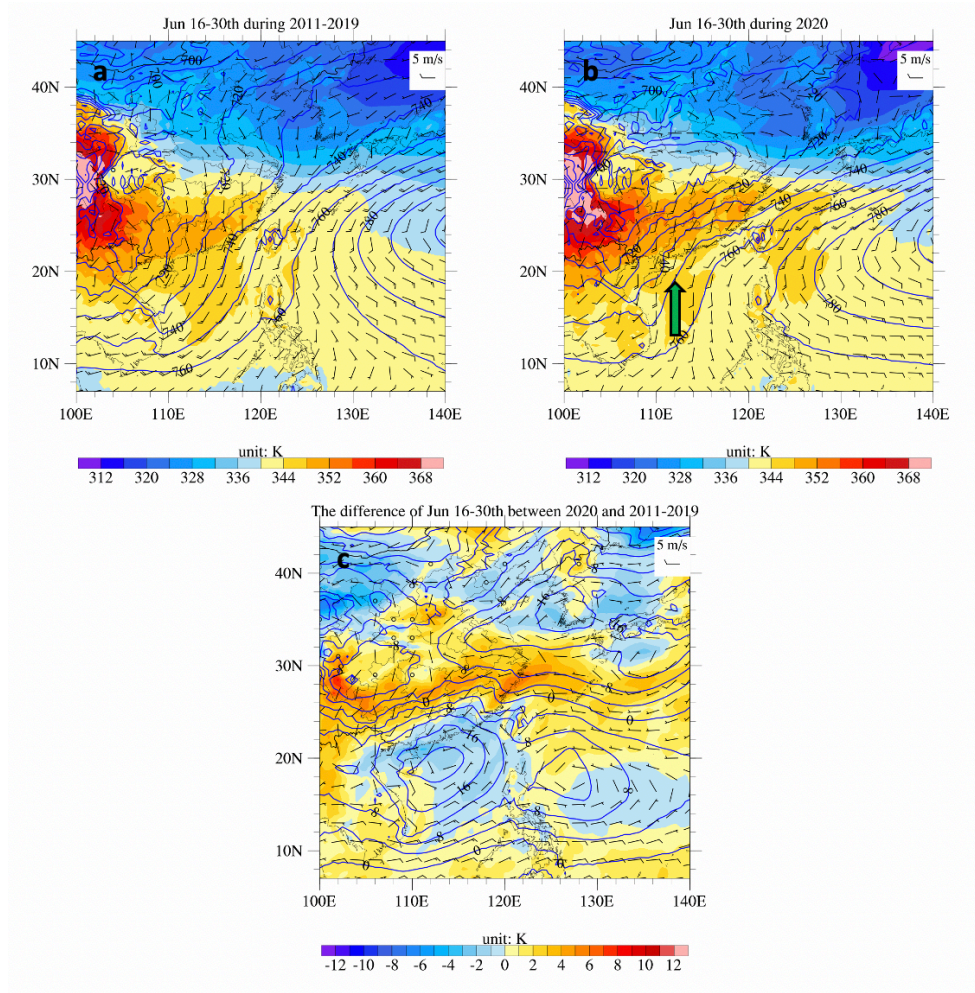


Figure 3. June 16 – June 30 CFSR 15-Days Average (a) composite map of the 925-hPa winds (m/s), geopotential height (gpm) and equivalent potential temperature (K) for the 2011-2019 ten-year mean conditions. (b) As in (a) but for the 2020. (c) Difference in wind (m/s), geopotential height (gpm) and equivalent potential temperature (K) between 2020 and 2011-2019 long term mean conditions.

When compared with the ten-year (2011-2019) mean conditions, the low-level geopotential height field (Fig. 2c,3c,4c,5c) shows that the WPSH has stronger intensity (> 36 gpm)

than normal. The 760 gpm line at the 925-hPa level (Fig. 2b,3b,4b,5b) which is usually located east of Taiwan around 125°E has already jumped to the southern China coastal area (113°E) and passed across the Taiwan Strait. In the meantime, its ridge axis is about 4 degrees north of its normal location during 1-15 June but is 4 degrees south of its normal position in late July. As a result, the onset of the Mei-Yu season starts early and ends late for a total of 62 days as compared to the normal Mei-Yu cases. From the geopotential height anomalies at 925-hPa (Figs. 2c-5c), it is obvious that the WPSH has westward extension and strength increase within the whole troposphere.

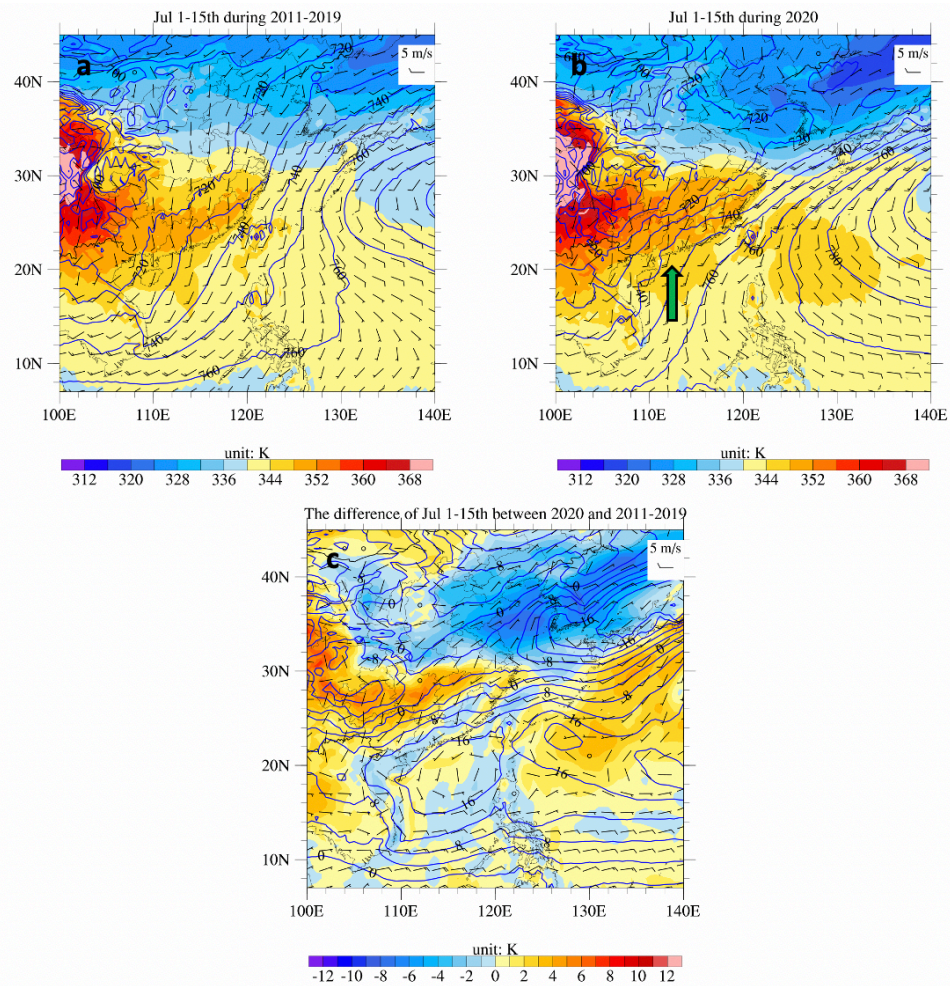


Figure 4. July 1 – July 15 CFSR 15-Days Average (a) composite map of the 925-hPa winds (m/s), geopotential height (gpm) and equivalent potential temperature (K) for the 2011-2019 ten-year mean conditions. (b) As in (a) but for the 2020. (c) Difference in wind (m/s), geopotential height (gpm) and equivalent potential temperature (K) between 2020 and 2011-2019 long term mean conditions.

By taking the air moisture into consideration (Figs. 2-5), the distribution of equivalent potential temperature and its anomalies highly indicates that the Yangtze River Valley regions in the central China Plain have greater concentration of water vapor in the air when compared with the previous Mei-Yu season during the same time. On the contrary, the low-level air masses above the South China Sea has less moisture inside due to the compression of WPSH with warm and dry air inside. The equivalent potential temperature inside the lee-side low-pressure system (SWV) (30°N , 116°E) (Figs. 2-5) along the front still shows the similar pattern with the ten-year mean conditions, consisting of warm and moist air inside. The deepening of this Mei-Yu frontal low-pressure system is largely related to the moist baroclinic process which is dominated by the latent heat release inside the vortex (Chen and Chen, 1995).

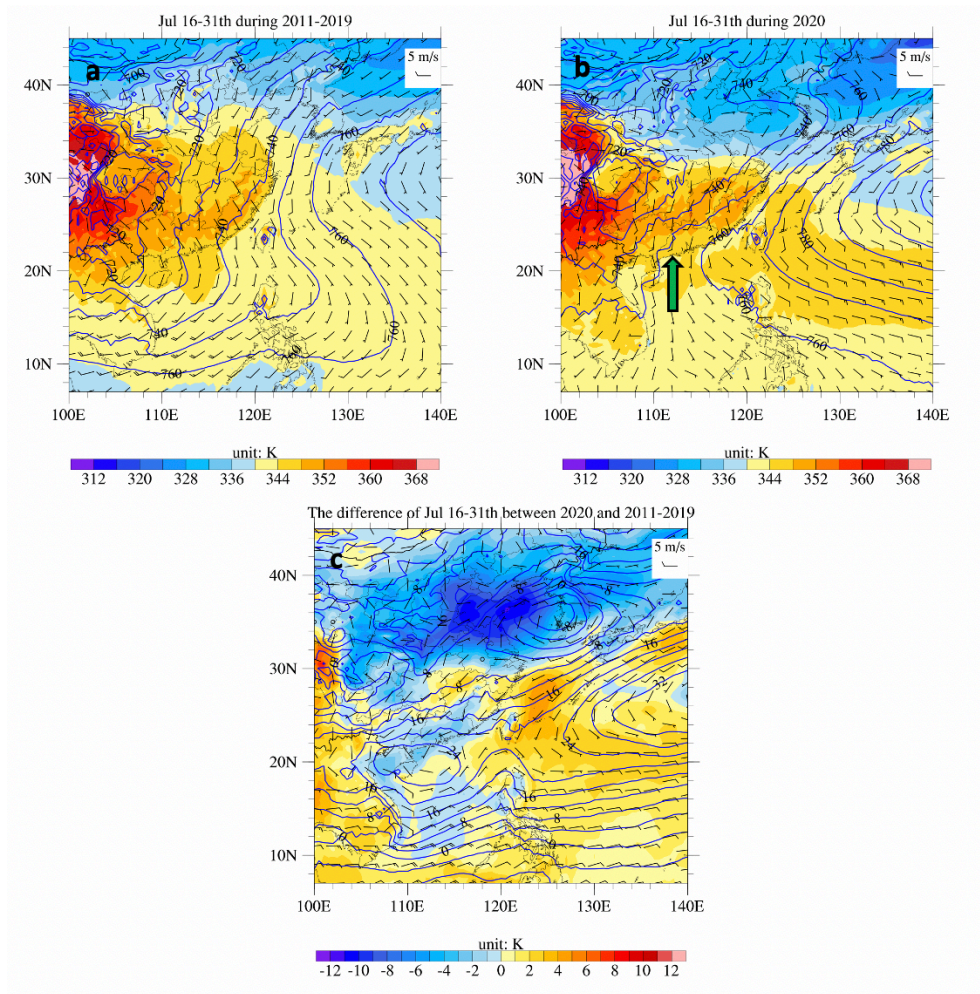


Figure 5. July 16 - July 31 CFSR 15-Days Average (a) composite map of the 925-hPa winds (m/s), geopotential height (gpm) and equivalent potential temperature (K) for the 2011-2019 ten-year mean conditions. (b) As in (a) but for the 2020. (c) Difference in wind (m/s), geopotential height (gpm) and equivalent potential temperature (K) between 2020 and 2011-2019 long term mean conditions.

Except for the equivalent potential temperature and pressure field positive anomalies, the low-level winds within the boundary layer (below 900-hPa) (Figs. 2-5) are also largely shifting northward especially over the South China Sea where the border region between SWV and WPSH is. As a result, in order to satisfy the geostrophic balance, a low-level wind maximum area (indicated by the green arrow) can be found over the South China Sea that is close to the Hainan Island. This low-level jet within the boundary layer is referred to as Marine Boundary Layer jet (MBLJ) in previous study (Chen et al. 2018, Tu et al. 2019, Tu et al. 2020) but shows different directions and locations over the nearly same ocean area.

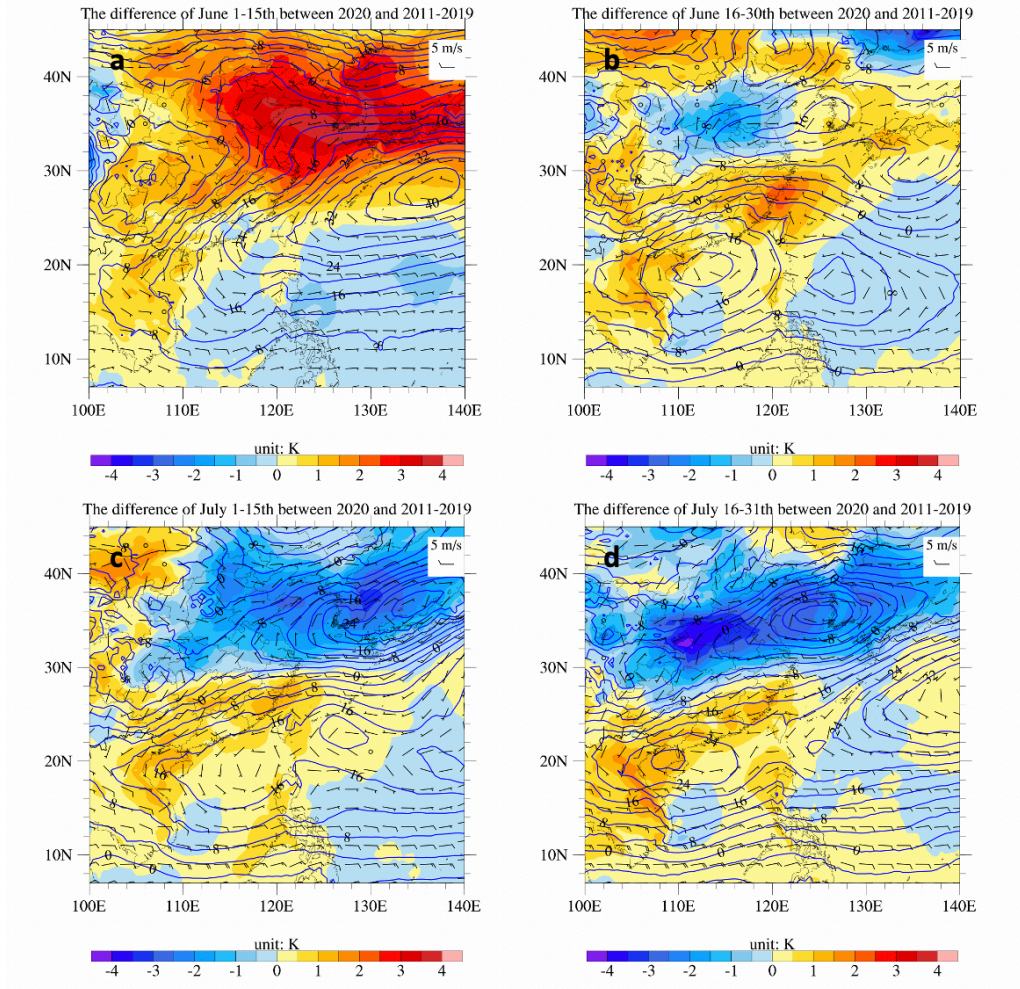


Figure 6. CFSR 15-Days Average (a) June 1 – June 15 composite map of 925-hPa winds anomalies (m/s), geopotential height anomalies (gpm), potential temperature anomalies (K) between 2011-2019 ten-year mean conditions and 2020. (b) As in (a) but for June 16 – June 30. (c) As in (a) but for July 1 – July 15. (d) As in (a) but for July 16 – July 31.

According to the previous studies for MBLJ by [Tu et al. \(2019\)](#), the prerequisite weather condition for MBLJ formation is the strong horizontal pressure gradient over South China Sea between the border region of a stronger WPSH and a South-West Vortex (SWV) after moving out of its origin place. The South-West Vortex is a low-pressure system that forms on the lee side of Tibet Plateau or Yun-Gui Plateau as lee-side cyclogenesis effect. The SWV usually shows its active performance during the summer rainy seasons, accompanied with the eastward movement out of the Sichuan Basin ([Chen and Chen, 1995](#)). The SWV system that moving out of its origin place is located on the opposite side of the subtropical high-pressure system in the Northwest

Pacific in summer, and sometimes it contributes to a strong pressure gradient formation at the junction region as a result (Tu et al. 2019). The MBLJ in their study is responsible for those heavy precipitation along the coastal area of Taiwan and southern China coastal area which might be overlooked by numerical weather forecasting as a result of its low-level spatial characteristics. During the Mei-Yu season 2020, the WPSH shows extremely strength while the lee-side low-pressure system (SWV) also has stronger than usual depth and active eastward-moving performance during the whole Mei-Yu season (Figs. 2-5). Those two weather systems both show anomalies in its' strength or location which will cause the MBLJ variation indirectly.

In addition, the anomalies of potential temperature at 925-hPa level (Fig. 6) clearly depict the cold polar air masses invading the southern China plain from mid-June to late July which largely contribute to the strong thermal gradient building up over the Yangtze River Valley. Both the cold polar air masses and the warm moist air flow from the ocean exhibit greater strength when compared with the long term mean conditions (Fig. 6). As a result, there is no doubt that the Mei-Yu precipitation along the front over Yangtze River Valley has stronger intensity during this time. This strong thermal contrast between those two different air masses will also contribute to the existence of thermal wind and secondary frontal circulation with relatively strong baroclinity along the Mei-Yu front.

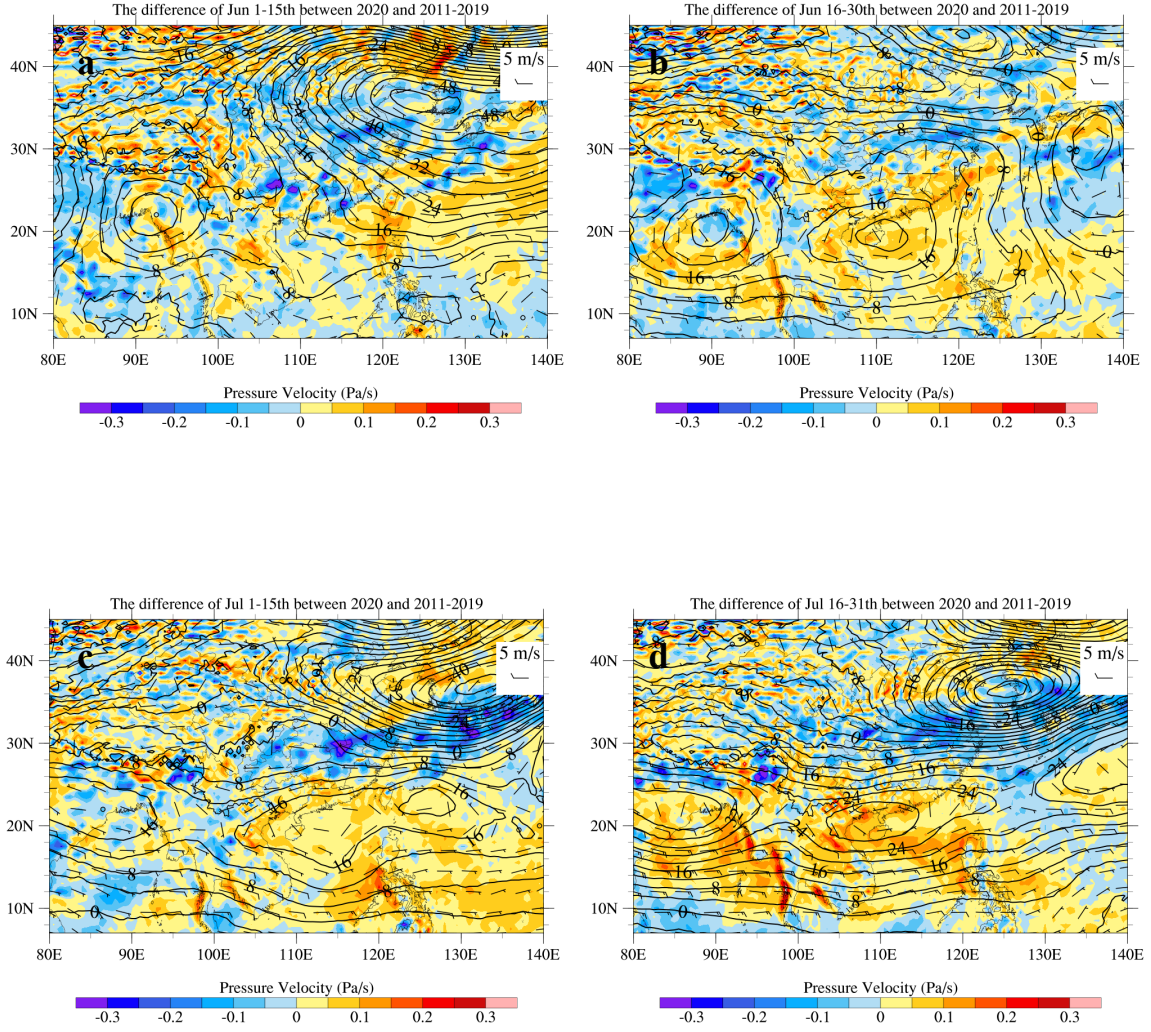


Figure 7. 15-days Average CFSR composite map of 500-hPa winds anomalies (m/s), geopotential height anomalies (gpm) and vertical pressure velocity anomalies (pa/s) for (a)June 1 – June 15. (b)June 16 – June 30. (c)July 1 – July 15. (d)July 16 – July 31.

As for the mid and upper-level circulations, the influence range of WPSH extends to the central part of Southern China Plain. Compared with the past ten-year mean conditions, the geopotential height anomalies at 500-hPa shows its positive maximum ($> 16gpm$) over the South China Sea (Fig. 7), this relatively stronger subtropical high-pressure system at the mid-level may contribute to the strong pressure gradient at a lower level when it encounters strong South-West Vortex. It is worth mentioning that the Bengal Depression at 500-hPa (Fig. 7) around the Bay of Bengal became weaker than the annual mean conditions during the Mei-Yu season 2020. The Bengal Depression plays an important role in causing heavy precipitations along the coastal regions and it contributes to the warm and moist monsoon flow transport. Therefore, the relatively weaker Bengal Depression indicates that the atmospheric system there cannot provide enough energy to satisfy the lower-level moist transporting from the Indian Ocean to the southern China plain. On the other hand, the weakening low-pressure system near the Bay of Bengal also implies the strengthening of the westerly wind over the Tibet Plateau which will contribute to the leeside descending motion and SWV active performance as a result.

The anomalous low-pressure system variations at the lower-level (925-hPa) (Figs. 2-5) in the leeside of the Tibetan Plateau is related to stronger than normal westerly current at the 500-hPa. This relatively strong wester flow or thermal wind is mainly caused by the stronger N-S pressure gradients due to the colder than normal polar air masses from the north (Fig. 6) and the weaker Bay of Bengal depression (Fig. 7) over the Indian ocean after the onset of the Indian monsoon. In addition, during the Summertime rainy season of China, the strong latent heat release inside the Sichuan Basin controlled by the moist and warm advection from the southeastern flank and colder air masses from the north plays the dominant role in SWV active eastward-moving performance. Those weather patterns will further contribute to the low-level wind field and MBLJ variation over the South China Sea during the Mei-Yu season 2020.

3.3 The WPSH Anomalies

When it comes to the abnormal changes in WPSH, the El Nino phenomena could be taken into consideration. Previous studies by Wang, Wu and Fu, (2000) have shown that ENSO can affect the intensity of the next year's East Asian summer monsoon flow, whereas the Northwest Pacific Anticyclone (WNPNC) is a bridge between the ENSO phenomenon and East Asian climate anomalies (Wang, Wu and Fu, 2000). Based on the sea surface temperature, the Oceanic Nino Index (Nino 3.4 Index) for Central Pacific El Nino (5°S - 5°N, 170°W - 120°W) events is an important meteorology indicator that is used to determine the occurrence of El Nino event. During the 2019 winter season and 2020 early spring season, the Nino 3.4 index shows its value (0.5-0.69) slightly higher than the Nino 3.4 threshold (0.5) which indicates that the SST anomalies occurred over the central Pacific area during this period can satisfy the criteria for central Pacific type El Nino events. After reaching its maximum value in the early Spring 2020, the Nino 3.4 Index for MJJ period (May, June and July) finally decrease to negative value (-0.2) which is the ending signal of this El Nino Events. In Wang's study (Wang, Wu and Fu, 2000), due to the hysteresis of air-sea interaction, the anomalies sometimes could survive in late spring or possibly in early summer and consequently affect the rainfall along the East Asian subtropical front (Mei-Yu front) as a result. The ENSO phenomenon has an interannual variation which occurred every 4-5 years, and the unusual heavy Mei-Yu precipitation and WPSH anomalies occurred in the 2020 summer rainy season may not be pertinent to ENSO.

In addition to the possible influence of El Nino events, the existence of Madden-Julian Oscillation (MJO) occurred over the Indian Ocean may also be used to explain the WPSH variation this summer. According to the [MJO Monthly Report posted by the Climate Prediction Center \(NOAA\)](#) (Fig. 8) during the Mei-Yu season, the RMM index depicts the absence of a MJO in summer 2020 with only a slightly eastward propagation signal starting from the mid-July.

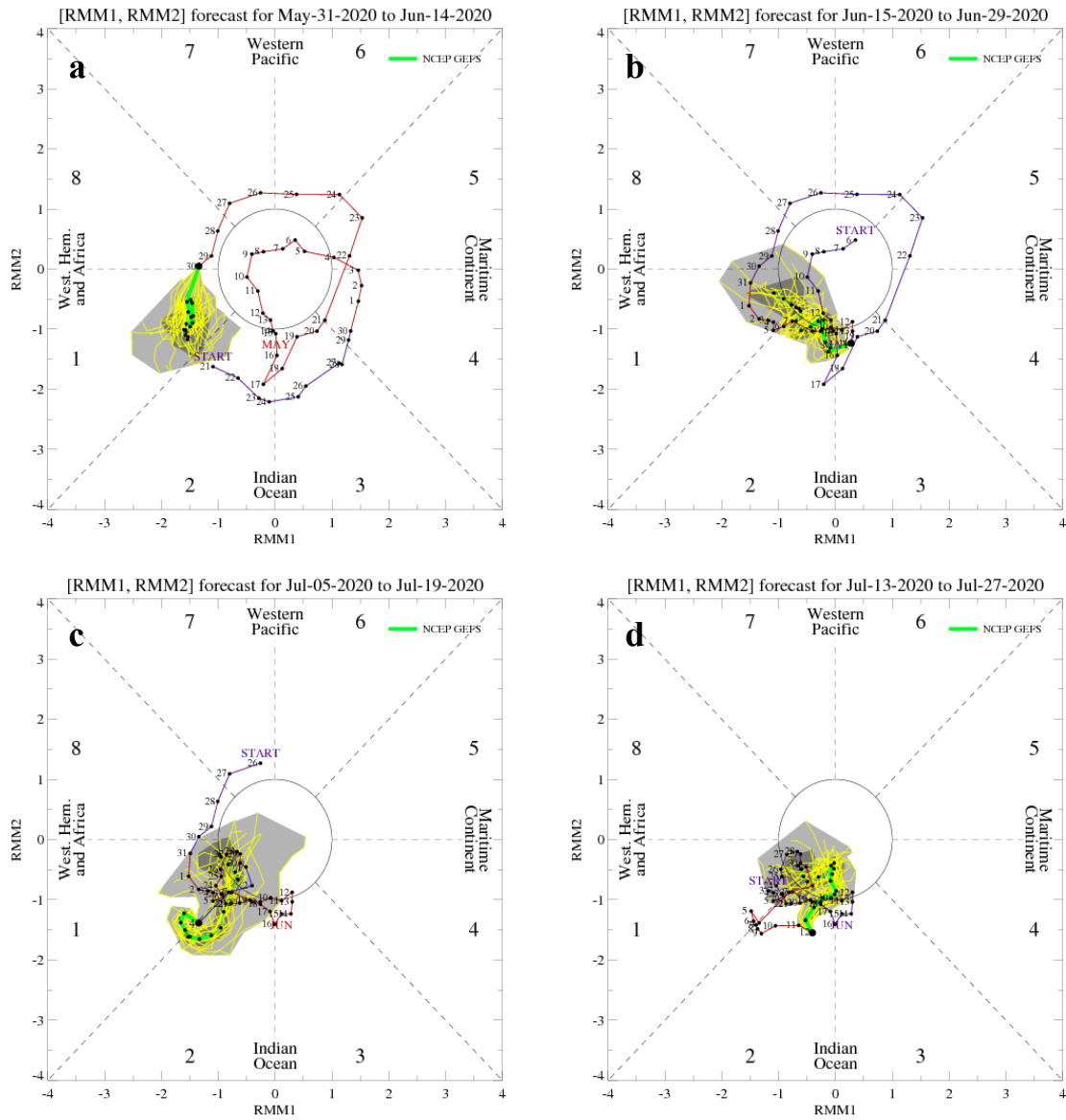


Figure 8. MJO Phase Evaluation during the Mei-Yu season 2020 obtained from the MJO Report prepared by the Climate Prediction Center (NCEP); The yellow line represents an ensemble member; the bold green line represents the ensemble mean and the light (dark) gray shading represents the area in which 50% (90%) of the ensemble members reside. (a) May 31 – June 14. (b) June 15 – June 29. (c) July 5 – July 19. (d) July 13 – July 27.

3.4 Moisture Transportation During the Mei-Yu Season 2020

During the early summer rainy season, the low-level moisture transport over the northern South China Sea occurs in the planetary boundary layer (Tu et al. 2019), often accompanied with heavy precipitation occurrences over the Taiwan area. The Mei-Yu rainy season over Taiwan is about one month earlier than the rainy season over the Yangtze River Valley of central China. From the horizontal distributions of Total Precipitable Water (TPW) (Fig. 9a,10a,11a,12a), it is clearly shown that there is a northeast-southwest tilting moist tongue extending from the northern South China Sea heading to the southern China coast and the Taiwan area with a maximum over southwestern China ahead of the SWV in June and early July.

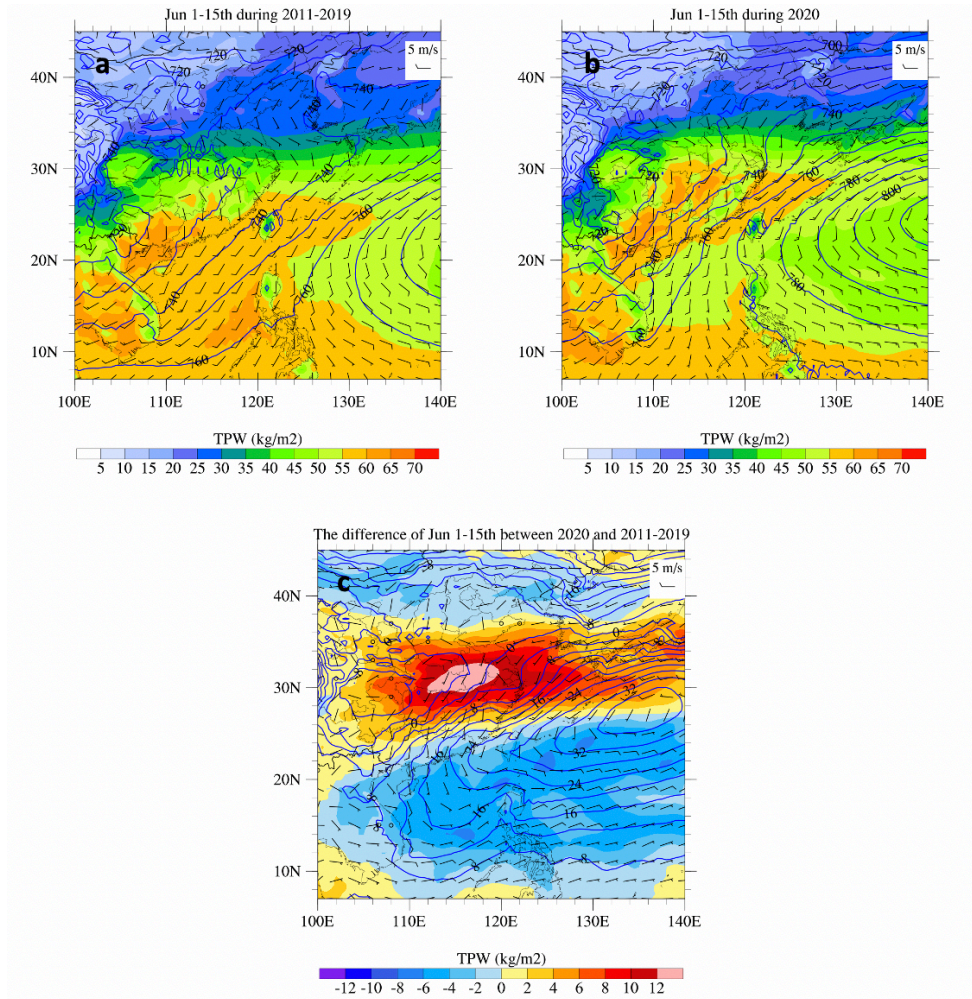


Figure 9. June 1 – 15 Average CFPSR (a) composite map of the 925-hPa winds (m/s), geopotential height (gpm) and TPW (mm) for the 2011-2019 ten-year mean conditions. (b) As in (a) but for the 2020. (c) Difference in wind (m/s), geopotential height (gpm) and TPW (mm) for the 2011-2019 ten-year mean conditions.

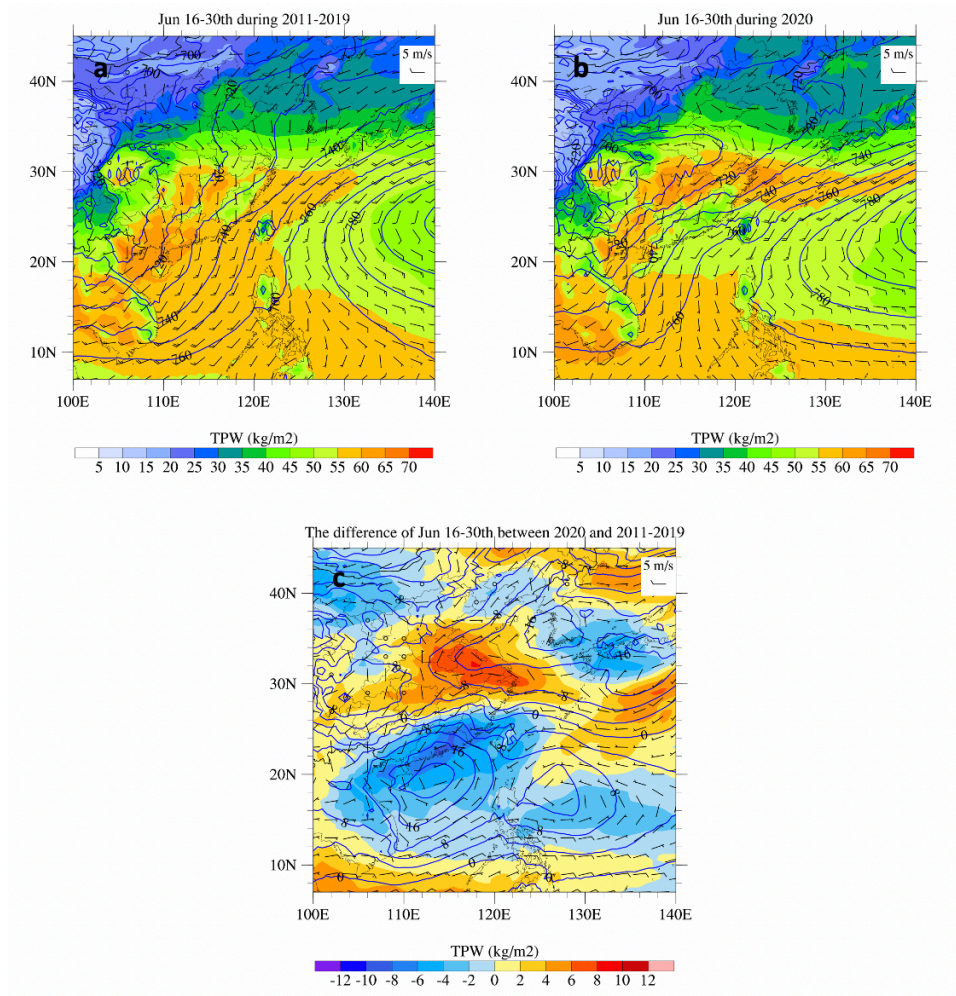


Figure 10. June 16-30 Average CFSR (a) composite map of the 925-hPa winds (m/s), geopotential height (gpm) and TPW (mm) for the 2011-2019 ten-year mean conditions. (b) As in (a) but for the 2020. (c) Difference in wind (m/s), geopotential height (gpm) and TPW (mm) between 2020 and 2011-2019 long term mean conditions.

During the 2020 Mei-Yu season, the moisture tongue shifted westward as compared with the ten-year (2011-2019) mean conditions with negative anomalies 4-8 mm over the northern South China Sea, Taiwan and southern China coast (Figs. 9b, 10b, 11b, 12b) which is related to stronger than normal WPSH that extended westward than its normal position. And the TPW anomalies (Fig. 9c, 10c, 11c, 12c) show extremely higher value of precipitable water concentrating over the Yangtze River Valley area with nearly west-east axis extending from the southern China plain to Japan and Korea during the entire Mei-Yu season.

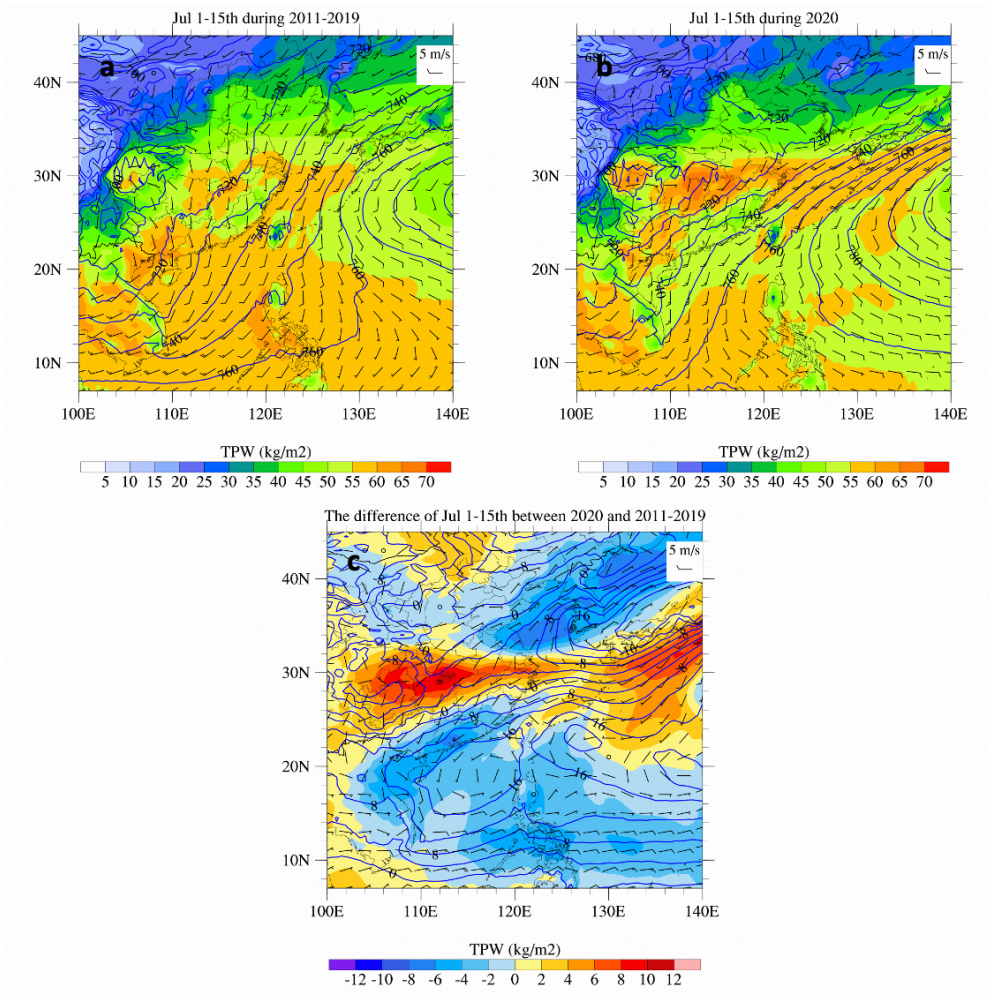


Figure 11. July 1-15 Average CFSR (a) composite map of the 925-hPa winds (m/s), geopotential height (gpm) and TPW (mm) for the 2011-2019 ten-year mean conditions. (b) As in (a) but for the 2020. (c) Difference in wind (m/s), geopotential height (gpm) and TPW (mm) between 2020 and 2011-2019 long term mean conditions.

Based on the low-level synoptic patterns, it is evident that the higher TPW over the Mei-Yu frontal zone over the Yangtze River Valley during 2020 Mei-Yu season is due to anomalous convergent airflow there (Figs. 9c, 10c, 11c, 12c) and is mainly caused by the vertical transport of the stronger rising motions. This issue will be further addressed from the horizontal moisture fluxes and moisture budget calculations in later section.

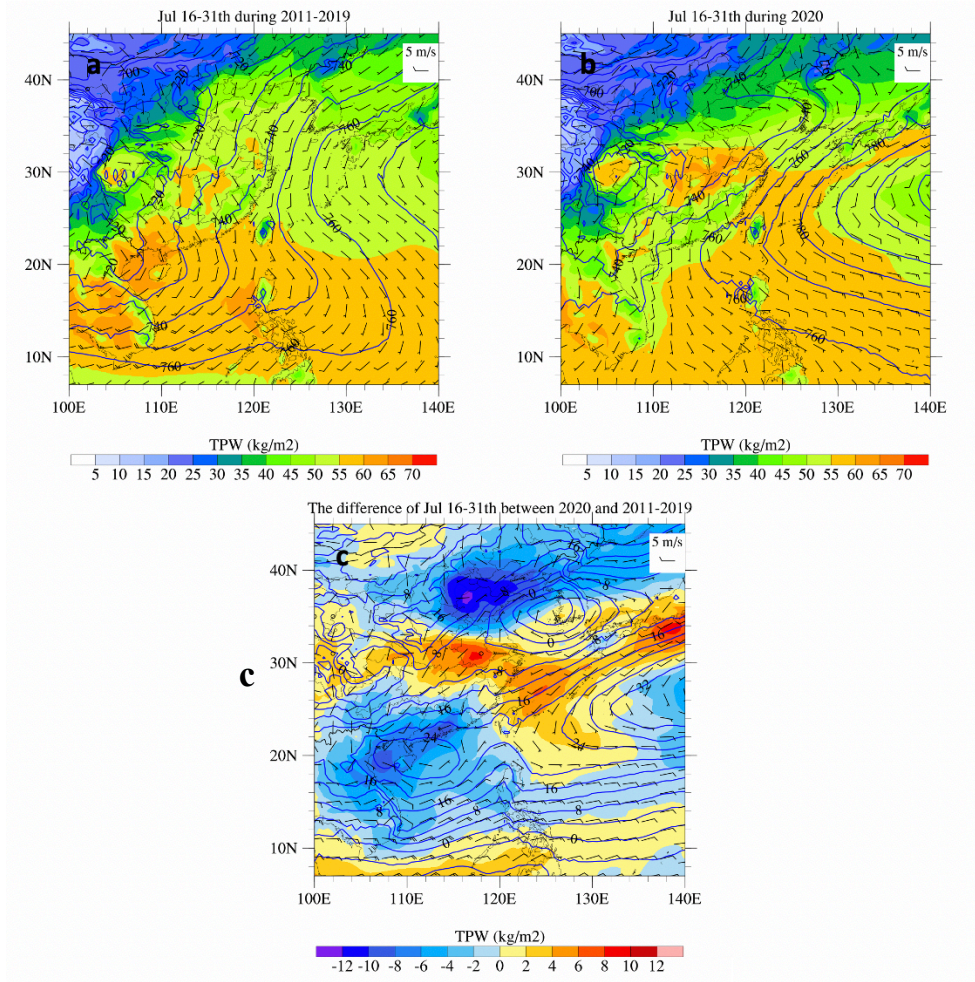


Figure 12. July 16-31 Average CFSR (a) composite map of the 925-hPa winds (m/s), geopotential height (gpm) and TPW (mm) for the 2011-2019 ten-year mean conditions. (b) As in (a) but for the 2020. (c) Difference in wind (m/s), geopotential height (gpm) and TPW (mm) between 2020 and 2011-2019 long term mean conditions.

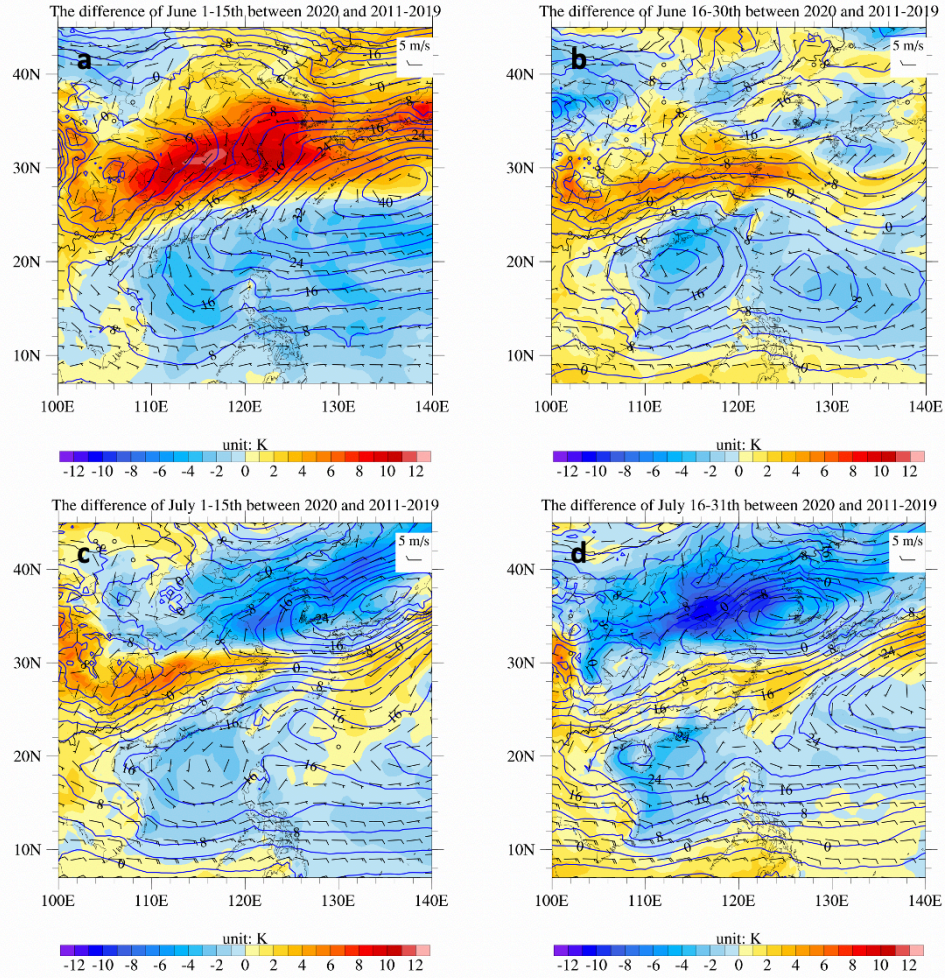


Figure 13. CFSR 15-Days Average (a) June 1 – June 15 composite map of 850-hPa winds anomalies (m/s), geopotential height anomalies (gpm), equivalent potential temperature anomalies (K) between 2011-2019 ten-year mean conditions and 2020. (b) As in (a) but for June 16 – June 30. (c) As in (a) but for July 1 – July 15. (d) As in (a) but for July 16 – July 31.

The horizontal “Q-flux” at lower atmospheric level (925-hPa and 850-hPa) (Fig. 14 and 15) indicate the existence of strong moist transport over the northern South China Sea at 925-hPa level and over the southern China Plain at a higher level (850-hPa) when it encountered the Mei-Yu front over southern China Plain. This is because of the terrain lifting effects over the southern China coastal region and Mei-Yu frontal lifting motion related to the secondary circulation (Chen et al, 1994; 1997) when the large horizontal moisture flux anomalies at the 850-hPa level (Fig. 15) are mainly confined over the southern China Plain. The anomalous moisture content (Fig. 13) associated with the rising motion in the frontal zone may also play a relatively important role in the atmospheric water vapor concentration over the southern China Plain. The baroclinicity across

the Mei-Yu frontal zone is more significant in 2020 than the 10-year mean with larger N-S thermal contrast across the frontal zone.

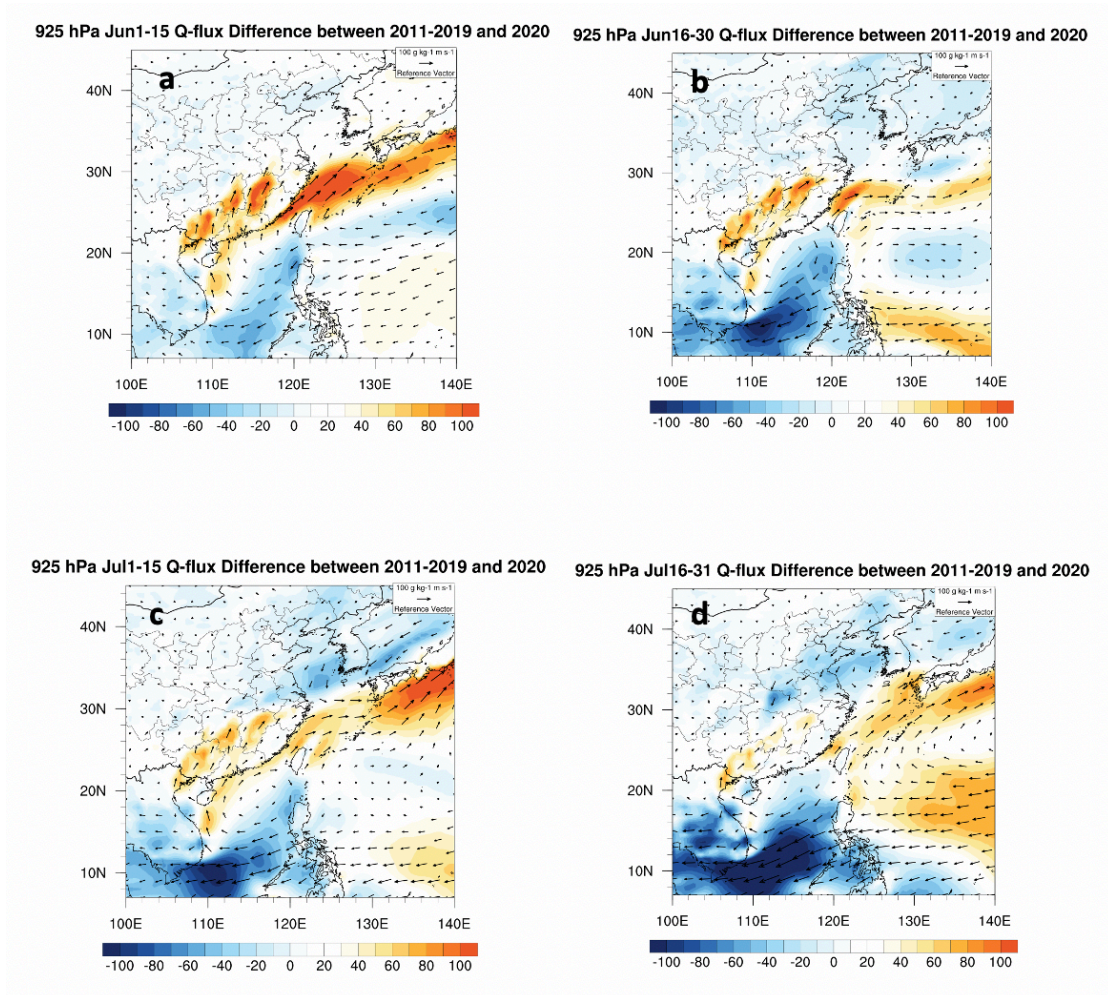


Figure 14. CFSR 15-Days Average (a) June 1 – June 15 composite map of 925-hPa “Q-flux” anomalies ($\text{g} \cdot \text{kg}^{-1} \cdot \text{m} \cdot \text{s}^{-1}$) between 2011–2019 ten-year mean conditions and 2020. (b) As in (a) but for June 16 – June 30. (c) As in (a) but for July 1 – July 15. (d) As in (a) but for July 16 – July 31.

The excessive moisture sources for heavy rainfall over the Yangtze River Valley during 2020 Mei-Yu season are mainly from the horizontal moisture transport within the marine boundary layer by the MBLJs (Figs. 16-19). The anomalous moisture transport by the MBLJ from the northern South China Sea split into two branches by the Hainan Island and diminished in later July.

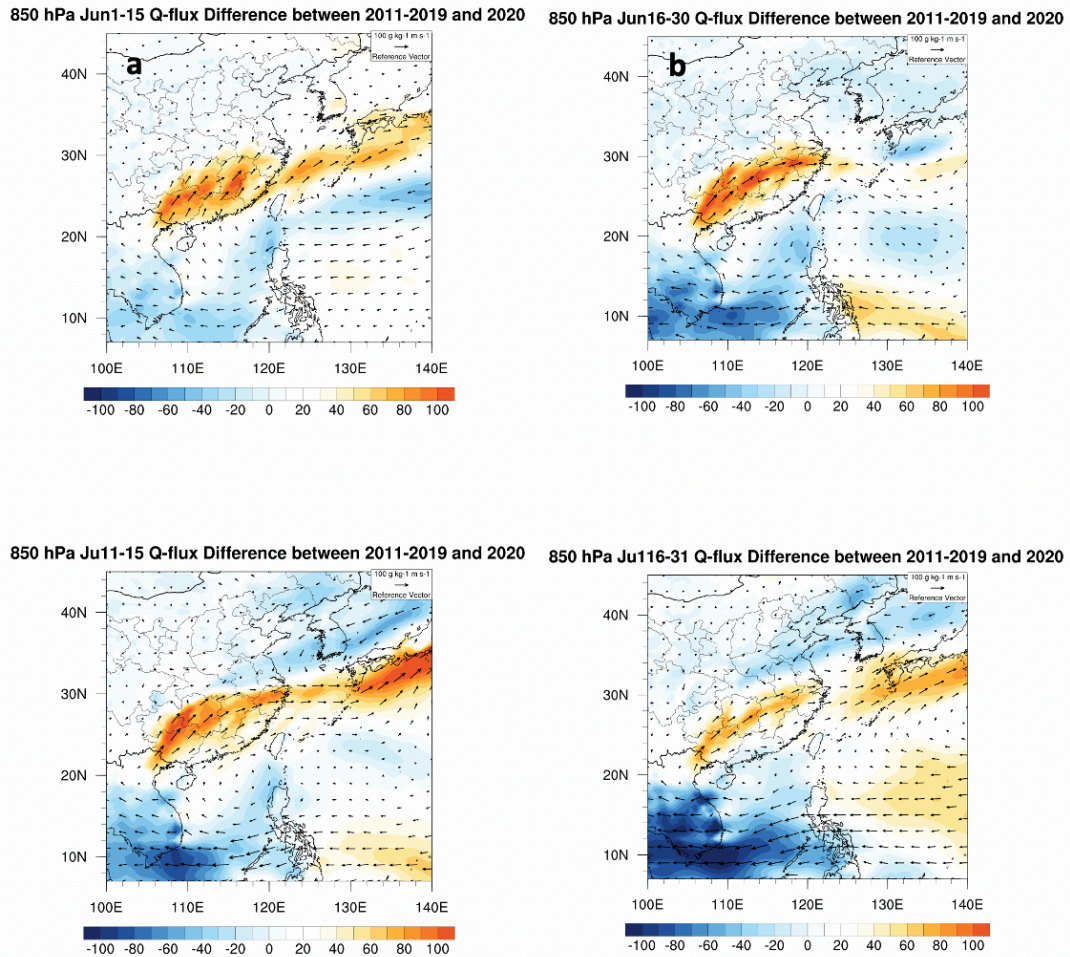


Figure 15. CFSR 15-Days Average (a) June 1 – June 15 composite map of 850-hPa “Q-flux” anomalies ($\text{g} \cdot \text{kg}^{-1} \cdot \text{m} \cdot \text{s}^{-1}$) between 2011-2019 ten-year mean conditions and 2020. (b) As in (a) but for June 16 – June 30. (c) As in (a) but for July 1 – July 15. (d) As in (a) but for July 16 – July 31.

Within the marine boundary layer (below 900-hPa), the large integrated vapor transport (IVT) (Fig. 16b,17b,18b,19b) during the 2020 Mei-Yu rainy season covering almost half of the southern China ocean area, demonstrates that the MBLJ plays an important role in low-level moisture transport with its maximum upstream of Hainan Island. The ten-year mean conditions of IVT based on the same period (Fig. 16a,17a,18a,19a) owes less due to weaker low-level southwesterly flow. While the IVT anomalies show the main moisture supply for the southern China plain during 2020 Mei-Yu season 2020 is from the northern South China Sea, it is carried northeastward with the strong low-level wind (MBLJ), contributing to the rainfall events over the

Yangtze River Valley. It is apparent that the moisture sources of the excessive rainfall for the 2020 Mei-Yu season over the Yangtze River Valley do not come from the Bay of Bengal.

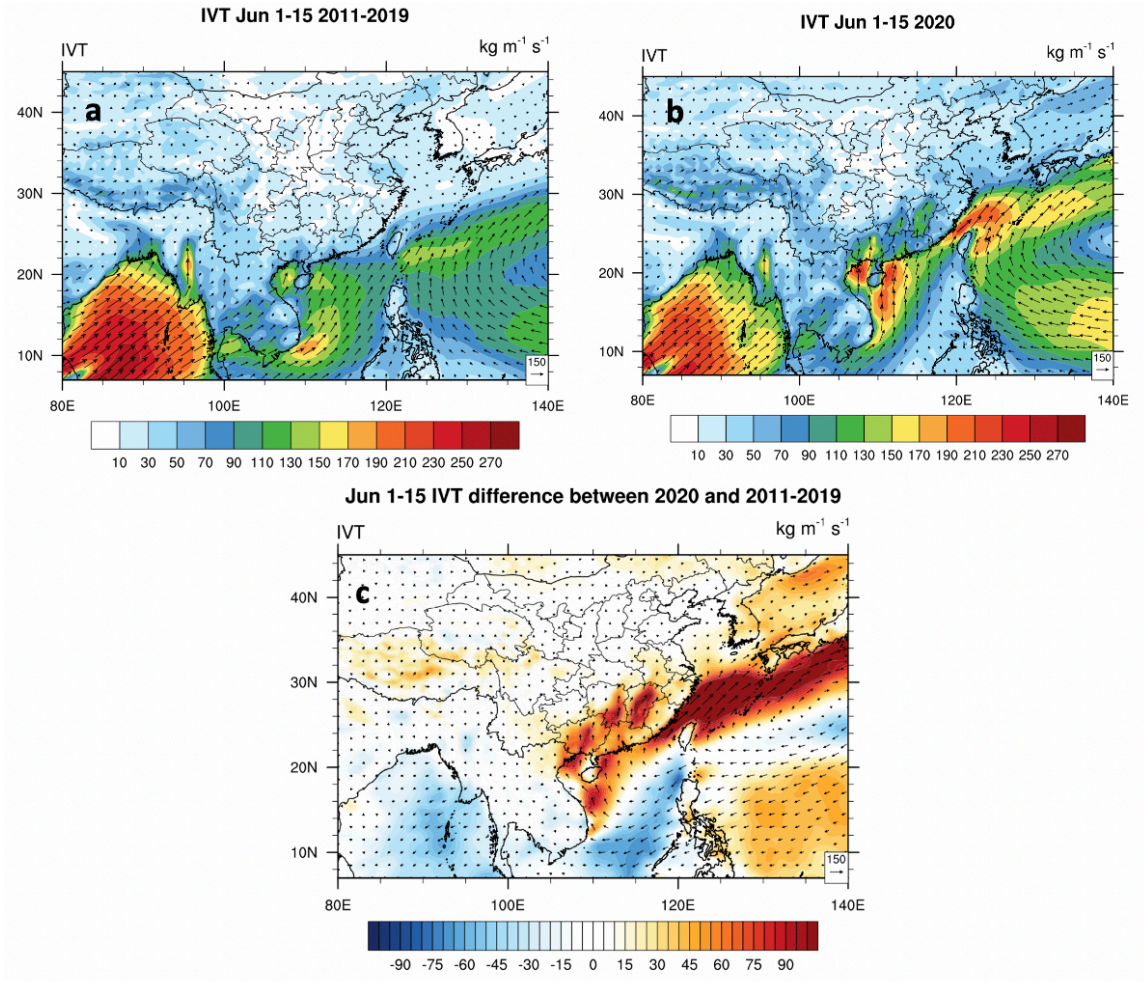


Figure 16. June 1-15 CFSR 15-days Average (a) IVT ($\text{kg} \cdot \text{m}^{-1} \cdot \text{s}^{-1}$) within the boundary layer (below 900-hPa) for 2011-2019 ten-year mean conditions. (b) As in (a) but for the 2020. (c) Difference in IVT ($\text{kg} \cdot \text{m}^{-1} \cdot \text{s}^{-1}$) between 2020 and 2011-2019 long term mean conditions.

Also, the moisture transport presented in Figures 16-19 is time averaged moisture fluxes calculated every 6 hours. To look into the contributions of moisture by the mean flow and transient eddies, I calculated the transport by the mean flow and subtracted it from the total transport calculated every 6 hours to obtain moisture transport by transient eddies. Figure 20 shows that the horizontal moisture fluxes in the planetary boundary layer from the northern South China Sea to the Yangtze River Valley are mainly contributed by the mean flow with negligible contributions

from transient flow (Fig. 20). It is evident that the prolonged excessive rainfall over the Yangtze River Valley during the 2020 Mei-Yu season is mainly related to anomalous mean flow patterns rather than transient disturbances. Over the southern Japan and southern Korea, the heavy rainfall is apparently related to the passage of transient disturbances, especially in June (Fig. 20). The Mei-Yu precipitation occurred over Yangtze River Valley in 2020 Mei-Yu season was relatively long-time weather phenomenon. On the contrary, the rainfall occurred over Japan and Korea during the 2020 Mei-Yu season is mainly caused by heavy rainfall events that only last for several hours within a few days.

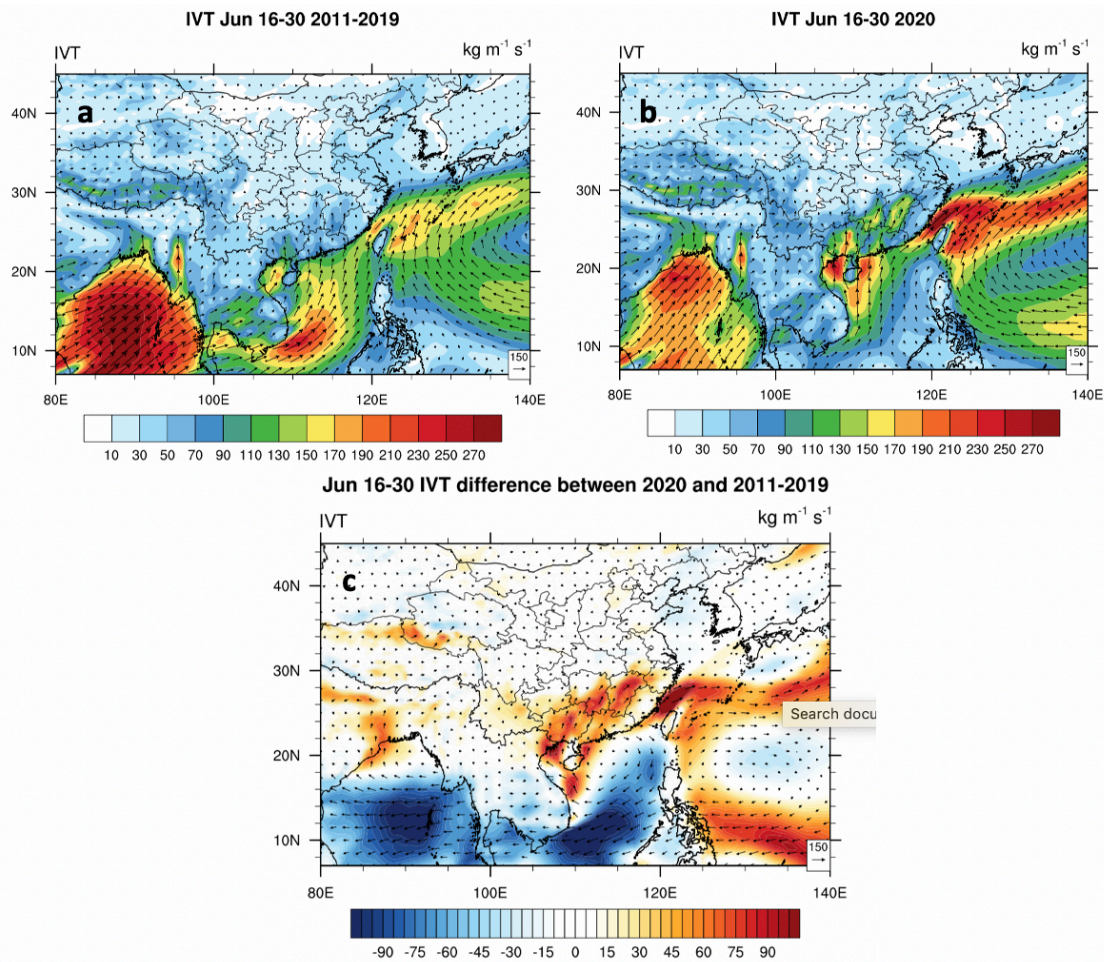


Figure 17. June 16-30 CFSR 15-days Average (a) IVT ($\text{kg} \cdot \text{m}^{-1} \cdot \text{s}^{-1}$) within the boundary layer (below 900-hPa) for 2011-2019 ten-year mean conditions. (b) As in (a) but for the 2020. (c) Difference in IVT ($\text{kg} \cdot \text{m}^{-1} \cdot \text{s}^{-1}$) between 2020 and 2011-2019 long term mean conditions.

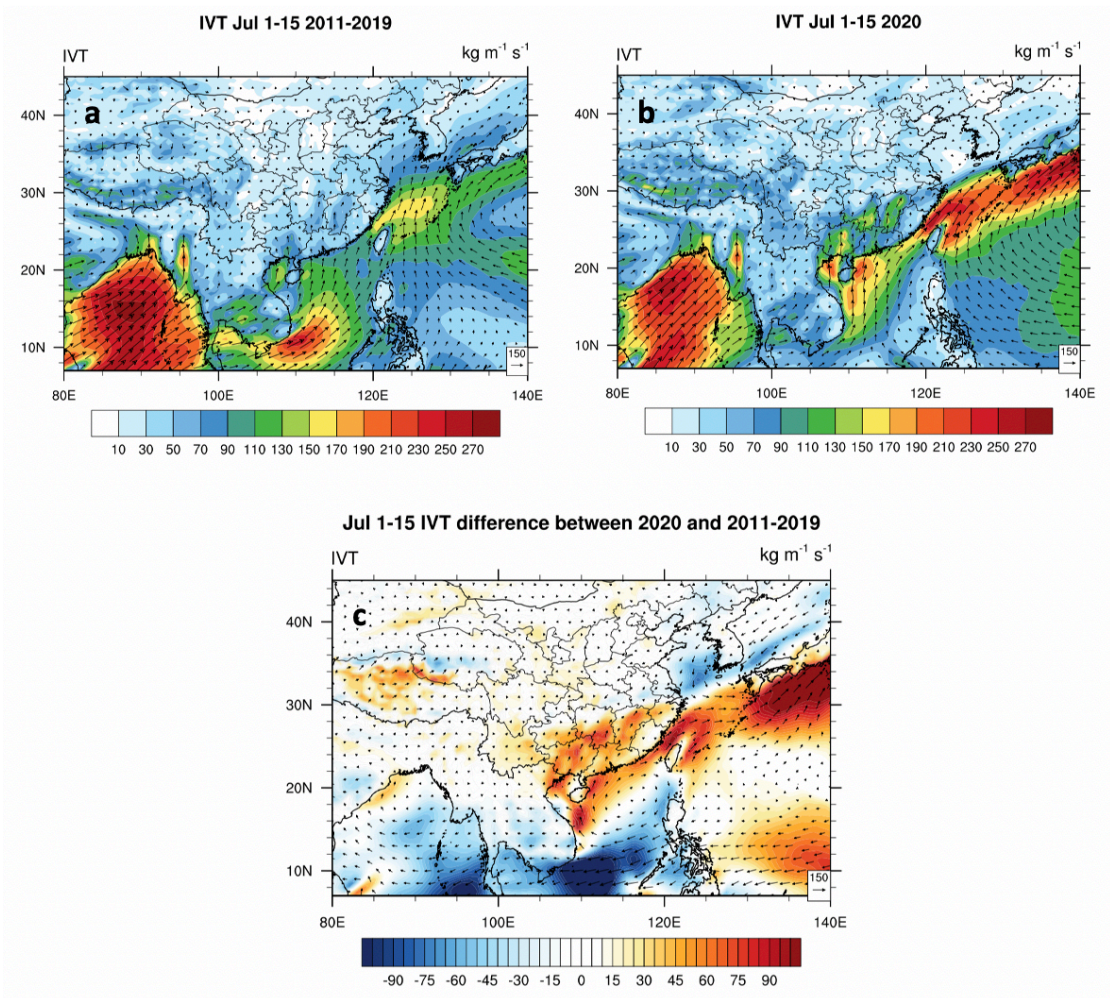


Figure 18. July 1-15 CFSR 15-days Average (a) IVT ($\text{kg} \cdot \text{m}^{-1} \cdot \text{s}^{-1}$) within the boundary layer (below 900-hPa) for 2011-2019 ten-year mean conditions. (b) As in (a) but for the 2020. (c) Difference in IVT ($\text{kg} \cdot \text{m}^{-1} \cdot \text{s}^{-1}$) between 2020 and 2011-2019 long term mean conditions

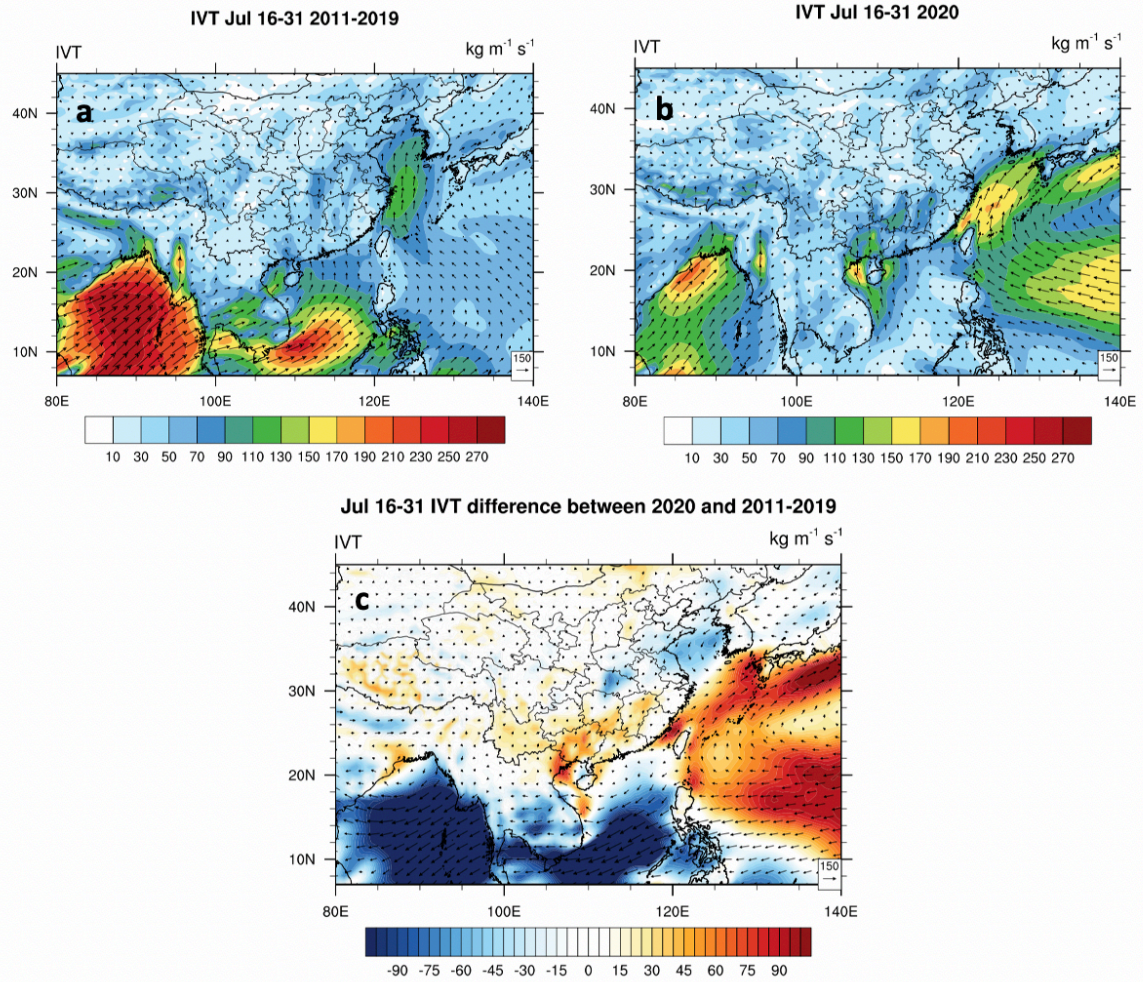


Figure 19. July 16-31 CFSR 15-days Average (a) IVT ($\text{kg} \cdot \text{m}^{-1} \cdot \text{s}^{-1}$) within the boundary layer (below 900-hPa) for 2011-2019 ten-year mean conditions. (b) As in (a) but for the 2020. (c) Difference in IVT ($\text{kg} \cdot \text{m}^{-1} \cdot \text{s}^{-1}$) between 2020 and 2011-2019 long term mean conditions.

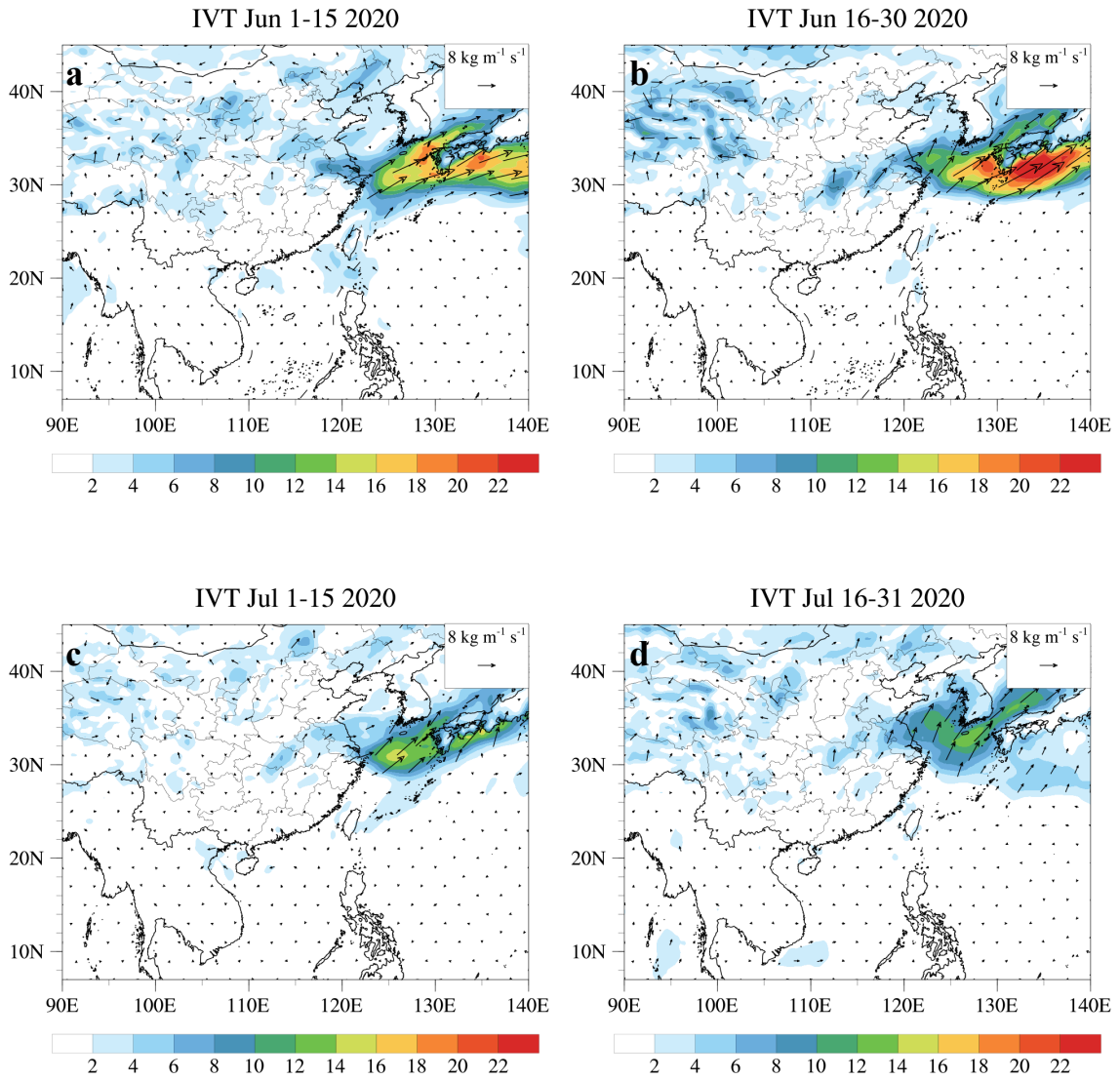


Figure 20. 2020 CFSR 15-days Average Transient IVT ($\text{kg} \cdot \text{m}^{-1} \cdot \text{s}^{-1}$) within the boundary layer (below 900-hPa) (a) June 1 – June 15. (b) June 16 – June 30. (c) July 1 – July 15. (d) July 16 – July 31.

3.5 The Synergistic Effect of SLLJ and MBLJ

This study has shown that during the 2020 Mei-Yu season, the MBLJ plays an important role in moisture transport from the northern South China Sea to the southern China Plain, and the transport is mainly maintained by the persistent mean flow. The excessive moisture content in the Mei-Yu frontal zone over the Yang-Tae Valley may be related to the strong convection associated with vertical frontal zone that brings the low-level moisture upward. The synergistic effect caused by SLLJ and MBLJ and moisture budget will be discussed in this section.

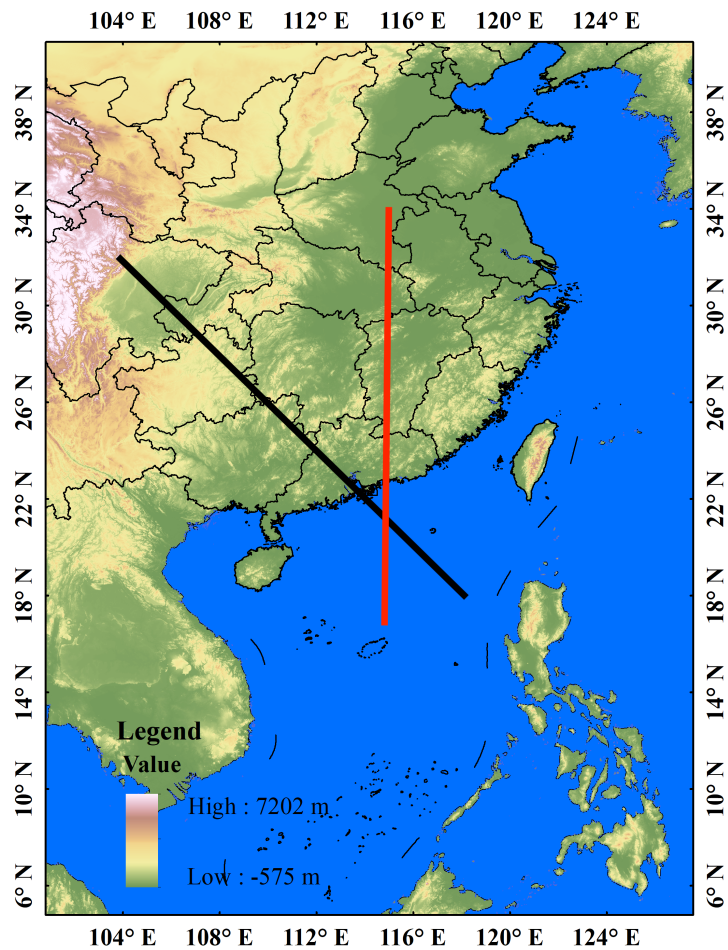


Figure 21. The position of tilting Cross-section axis (Black Solid Line) along (18°N, 118°E – 32°N, 104°E) and meridional cross-section axis (Red Solid Line) along (17°N, 115°E – 34°N, 115°E). The shading area indicates terrain height (m). The black solid line shows the location of cross-sections displayed in this section and the red solid line indicates the location of meridional cross-sections displayed in the Appendix.

According to the difference of “Q-flux” distribution at different levels (925-hPa and 850-hPa) (Fig. 14 and 15), it indicates that the horizontal moisture transport within the boundary layer from the northern South China Sea has been lifted up over the southern China Plain as a result of the terrain effect and frontal secondary circulation (Chen et al., 1994; 1997). In order to better depict the characteristics of MBLJ and its’ related moisture transport to the Yangtze River Valley, a vertical cross-section along the tilting axis ($18^{\circ}N, 118^{\circ}E - 32^{\circ}N, 104^{\circ}E$) has been taken into consideration. After ignoring the possible influence of coastal orographic blocking to a large extent, from the tilting axis cross-sections of horizontal wind and horizontal moisture flux along the tilting axis (Figs. 21-28), a strong boundary layer jet (below 900-hPa) ($> 10 \text{ ms}^{-1}$) can be found in front of the Hainan Island (around $20^{\circ}N$) accompanied with strong horizontal moisture flux ($> 160 \text{ g} \cdot \text{kg}^{-1} \cdot \text{ms}^{-1}$) when compared with the ten-year mean conditions over the same area. The low-level atmospheric wind field over the northern South China Sea shows an anomalous meridional over a wide area. Based on these findings, for the 2020 Mei-Yu season, the horizontal moisture was largely confined within the marine boundary layer and advected to the Mei-Yu frontal zone over the Yang-Tze Reiver Valley by the anomalous mean flow. The moisture sources are mainly from the northern South China Sea other than from the Bay of Bengal as suggested by previous studies (e.g., Chen and Yu 1988). Furthermore, we also think that the horizontal moisture transport was not by the SLLJ in the 850-700 hPa layer. Plots of vertical meridional cross-sections along $115^{\circ}E$ (Red Solid Line) are shown in the Appendix.

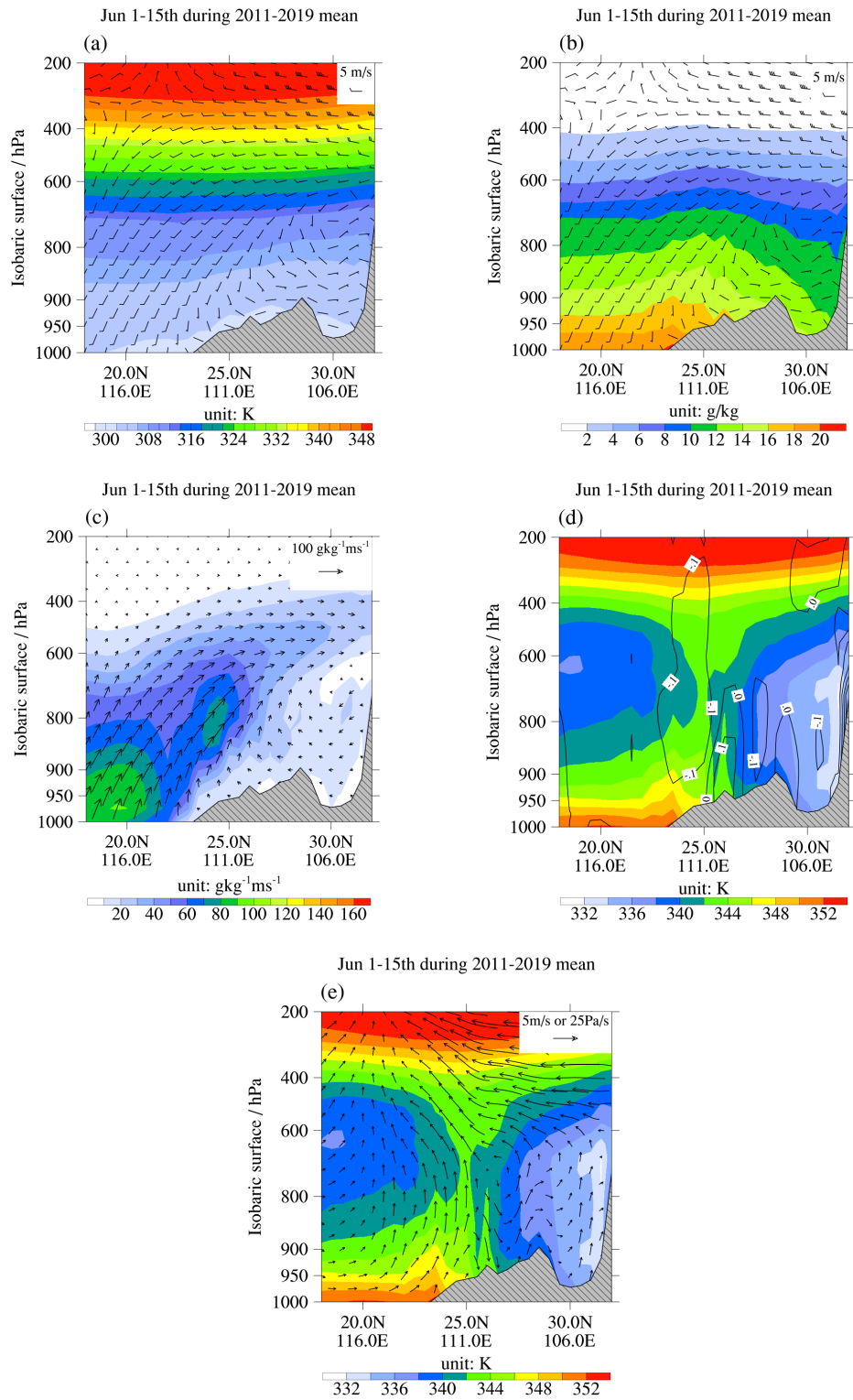


Figure 22. June 1-June 15. CFSR 15-days average cross-sections along ($18^{\circ}\text{N}, 118^{\circ}\text{E} - 32^{\circ}\text{N}, 104^{\circ}\text{E}$) for 2011-2019 ten-year mean. (a) Composite map of horizontal winds (m/s) and potential temperature (K). (b) Composite map of horizontal wind and specific humidity (g/kg). (c) Horizontal moisture flux ($\text{g} \cdot \text{kg}^{-1} \cdot \text{m} \cdot \text{s}^{-1}$). (d) Composite map of vertical velocity (pa/s) and equivalent potential temperature (K). (e) Composite map of atmospheric circulation and equivalent potential temperature (K). The grey shading area indicates terrain.

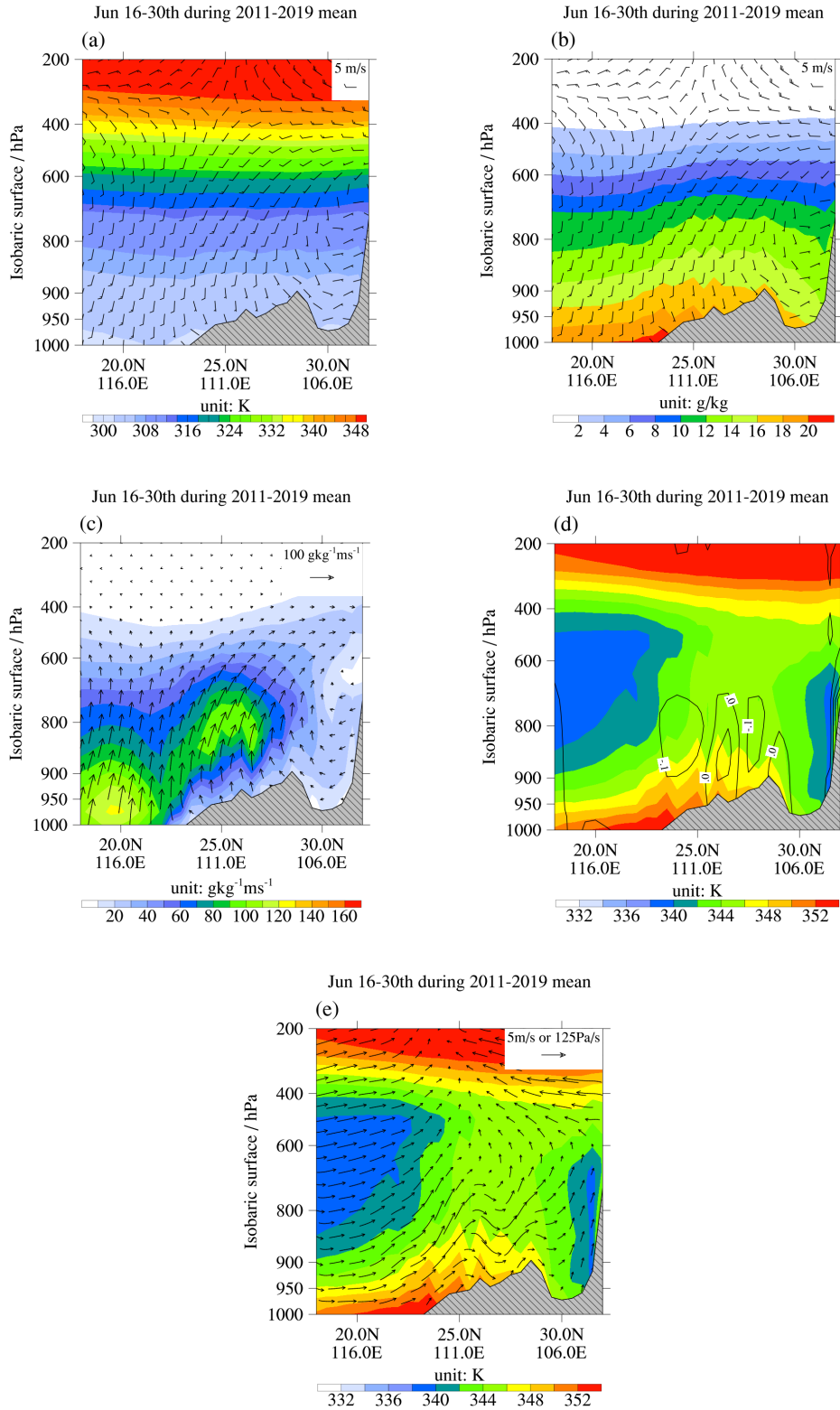


Figure 23. June 16-June 30. CFSR 15-days average cross-sections along ($18^{\circ}\text{N}, 118^{\circ}\text{E} - 32^{\circ}\text{N}, 104^{\circ}\text{E}$) for 2011-2019 ten-year mean. (a) Composite map of horizontal winds (m/s) and potential temperature (K). (b) Composite map of horizontal wind and specific humidity (g/kg). (c) Horizontal moisture flux ($\text{g} \cdot \text{kg}^{-1} \cdot \text{m} \cdot \text{s}^{-1}$). (d) Composite map of vertical velocity (pa/s) and equivalent potential temperature (K). (e) Composite map of atmospheric circulation and equivalent potential temperature (K). The grey shading area indicates terrain.

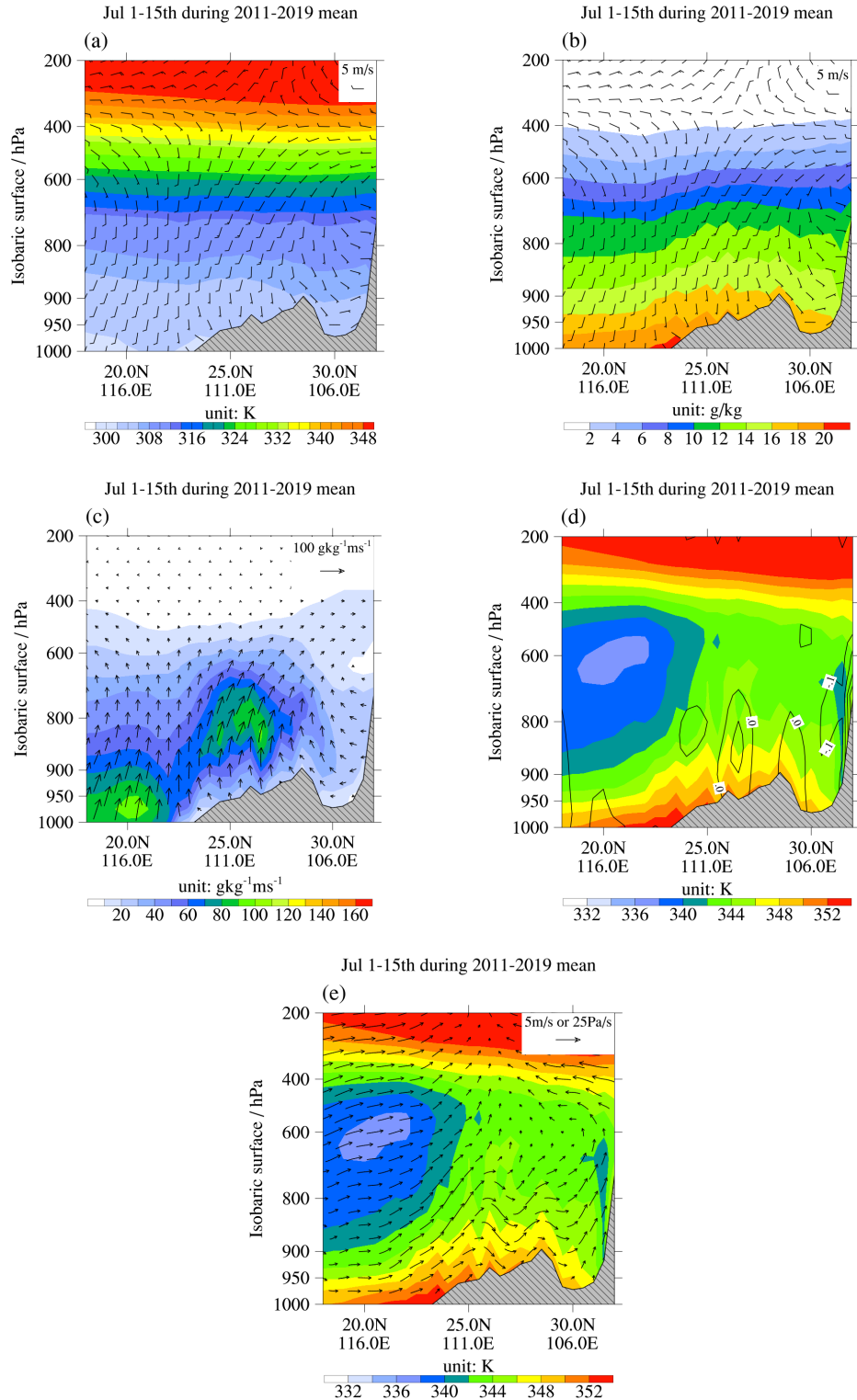


Figure 24. July 1-July 15. CFSR 15-days average cross-sections along ($18^{\circ}\text{N}, 118^{\circ}\text{E} - 32^{\circ}\text{N}, 104^{\circ}\text{E}$) for 2011-2019 ten-year mean. (a) Composite map of horizontal winds (m/s) and potential temperature (K). (b) Composite map of horizontal wind and specific humidity (g/kg). (c) Horizontal moisture flux ($\text{g} \cdot \text{kg}^{-1} \cdot \text{m} \cdot \text{s}^{-1}$). (d) Composite map of vertical velocity (pa/s) and equivalent potential temperature (K). (e) Composite map of atmospheric circulation and equivalent potential temperature (K). The grey shading area indicates terrain.

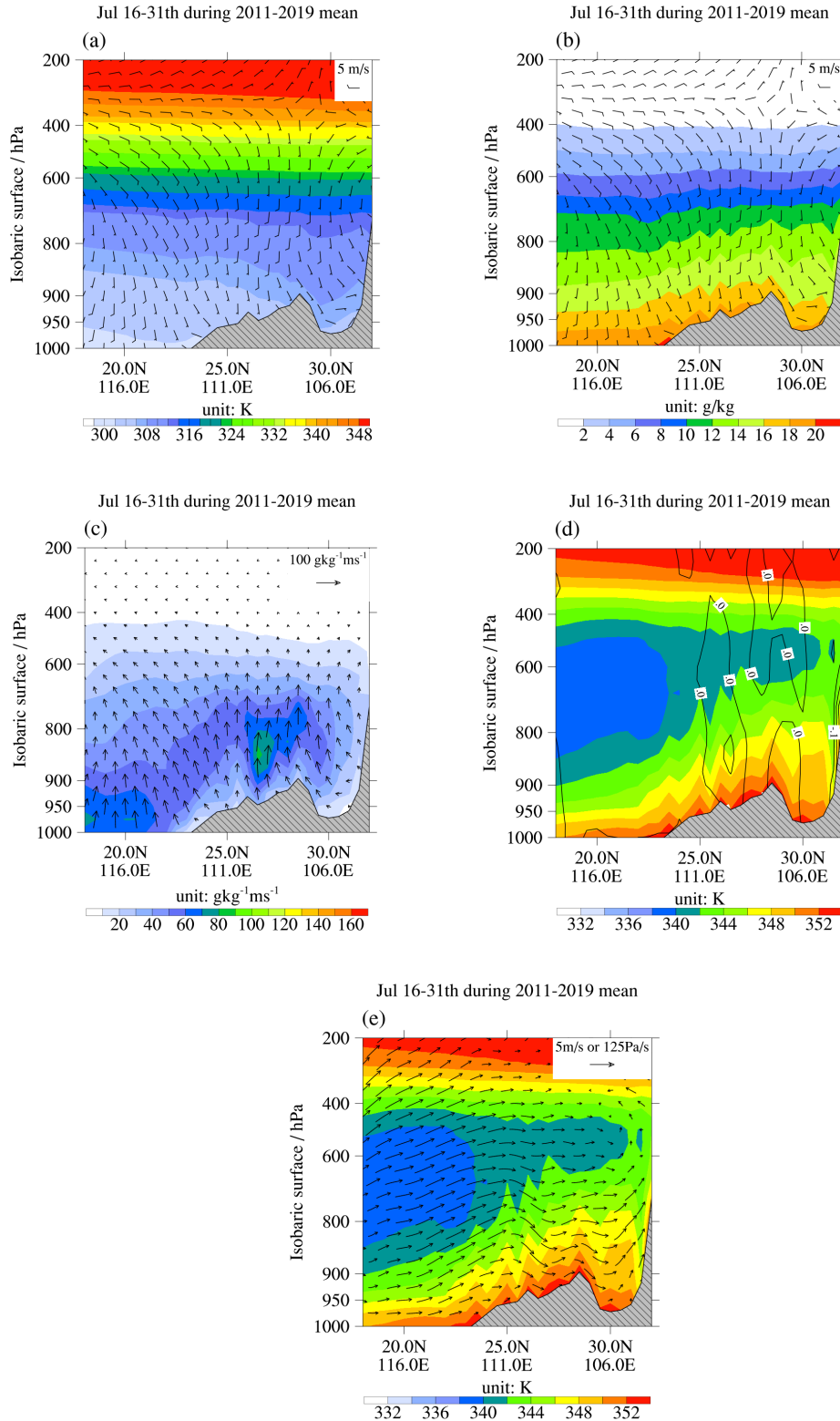


Figure 25. July 16-July 31. CFSR 15-days average cross-sections along ($18^{\circ}\text{N}, 118^{\circ}\text{E} - 32^{\circ}\text{N}, 104^{\circ}\text{E}$) for 2011-2019 ten-year mean. (a) Composite map of horizontal winds (m/s) and potential temperature (K). (b) Composite map of horizontal wind and specific humidity (g/kg). (c) Horizontal moisture flux ($\text{g} \cdot \text{kg}^{-1} \cdot \text{m} \cdot \text{s}^{-1}$). (d) Composite map of vertical velocity (pa/s) and equivalent potential temperature (K). (e) Composite map of atmospheric circulation and equivalent potential temperature (K). The grey shading area indicates terrain.

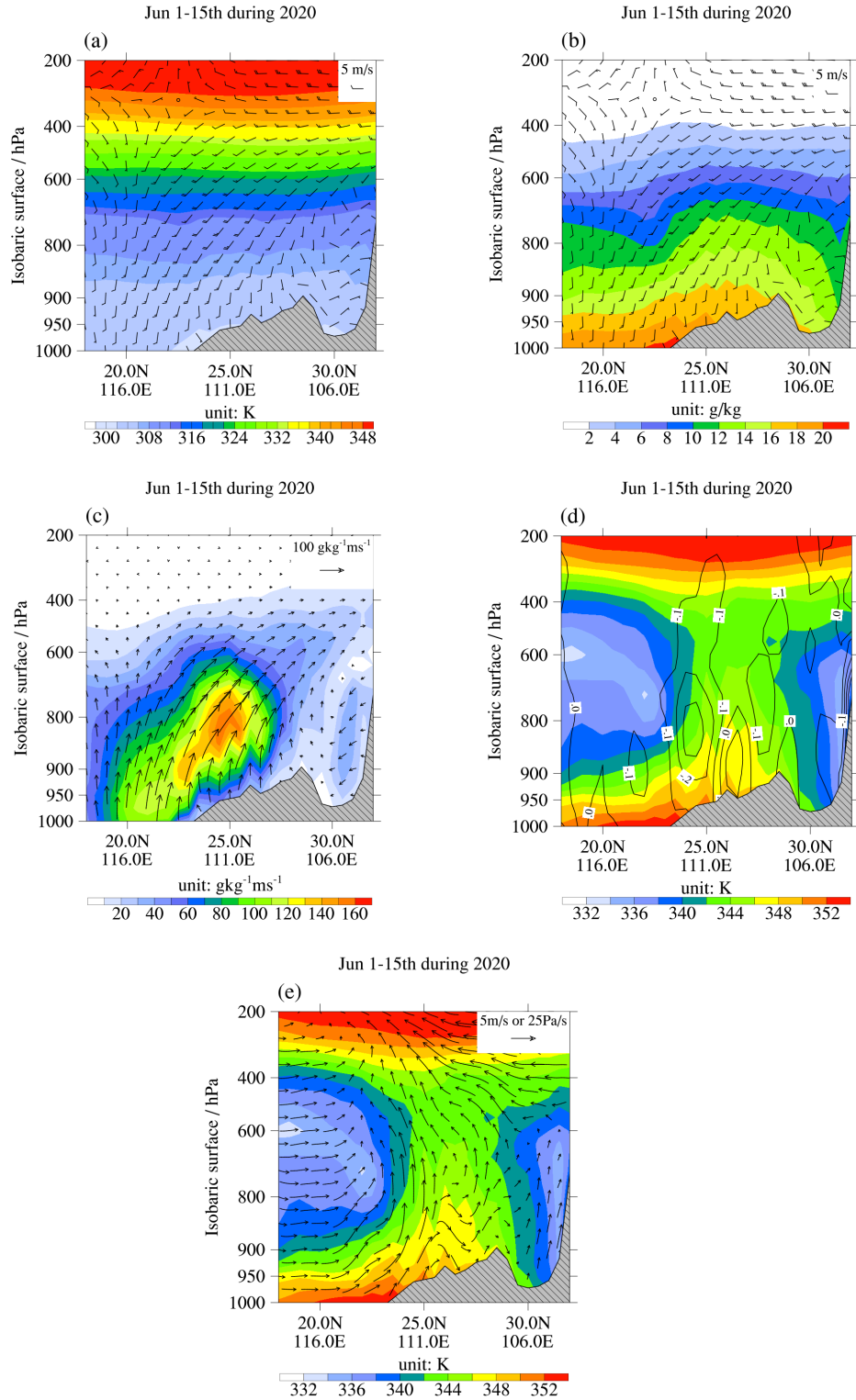


Figure 26. June 1-June 15. CFSR 15-days average cross-sections along ($18^{\circ}\text{N}, 118^{\circ}\text{E} - 32^{\circ}\text{N}, 104^{\circ}\text{E}$) for 2020. (a) Composite map of horizontal winds (m/s) and potential temperature (K). (b) Composite map of horizontal wind and specific humidity (g/kg). (c) Horizontal moisture flux ($\text{g} \cdot \text{kg}^{-1} \cdot \text{m} \cdot \text{s}^{-1}$). (d) Composite map of vertical velocity (pa/s) and equivalent potential temperature (K). (e) Composite map of atmospheric circulation and equivalent potential temperature (K). The grey shading area indicates terrain.

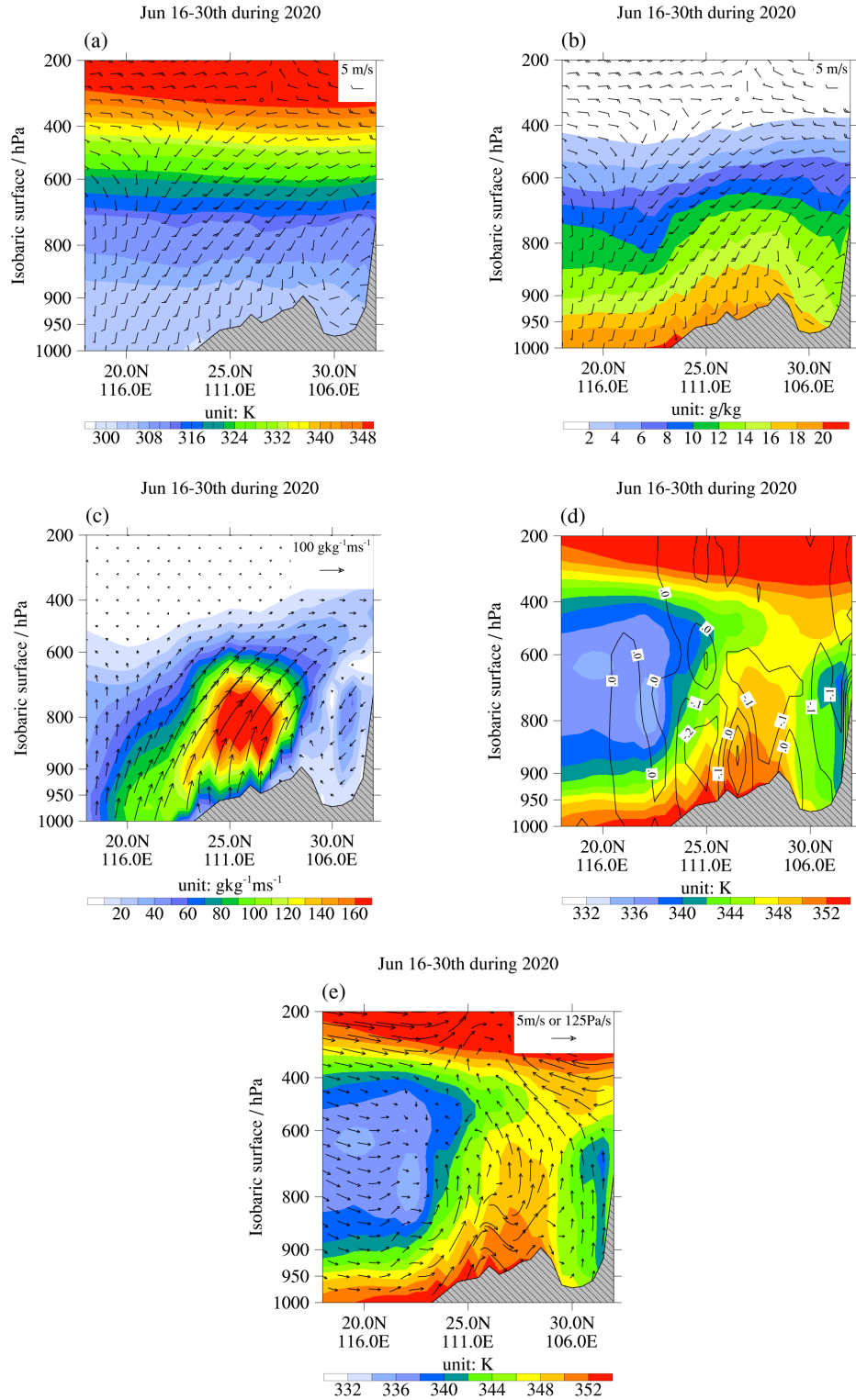


Figure 27. June 16-June 30. CFSR 15-days average cross-sections along (18°N, 118°E – 32°N, 104°E) for 2020. (a) Composite map of horizontal winds (m/s) and potential temperature (K). (b) Composite map of horizontal wind and specific humidity (g/kg). (c) Horizontal moisture flux ($\text{g} \cdot \text{kg}^{-1} \cdot \text{m} \cdot \text{s}^{-1}$). (d) Composite map of vertical velocity (pa/s) and equivalent potential temperature (K). (e) Composite map of atmospheric circulation and equivalent potential temperature (K). The grey shading area indicates terrain.

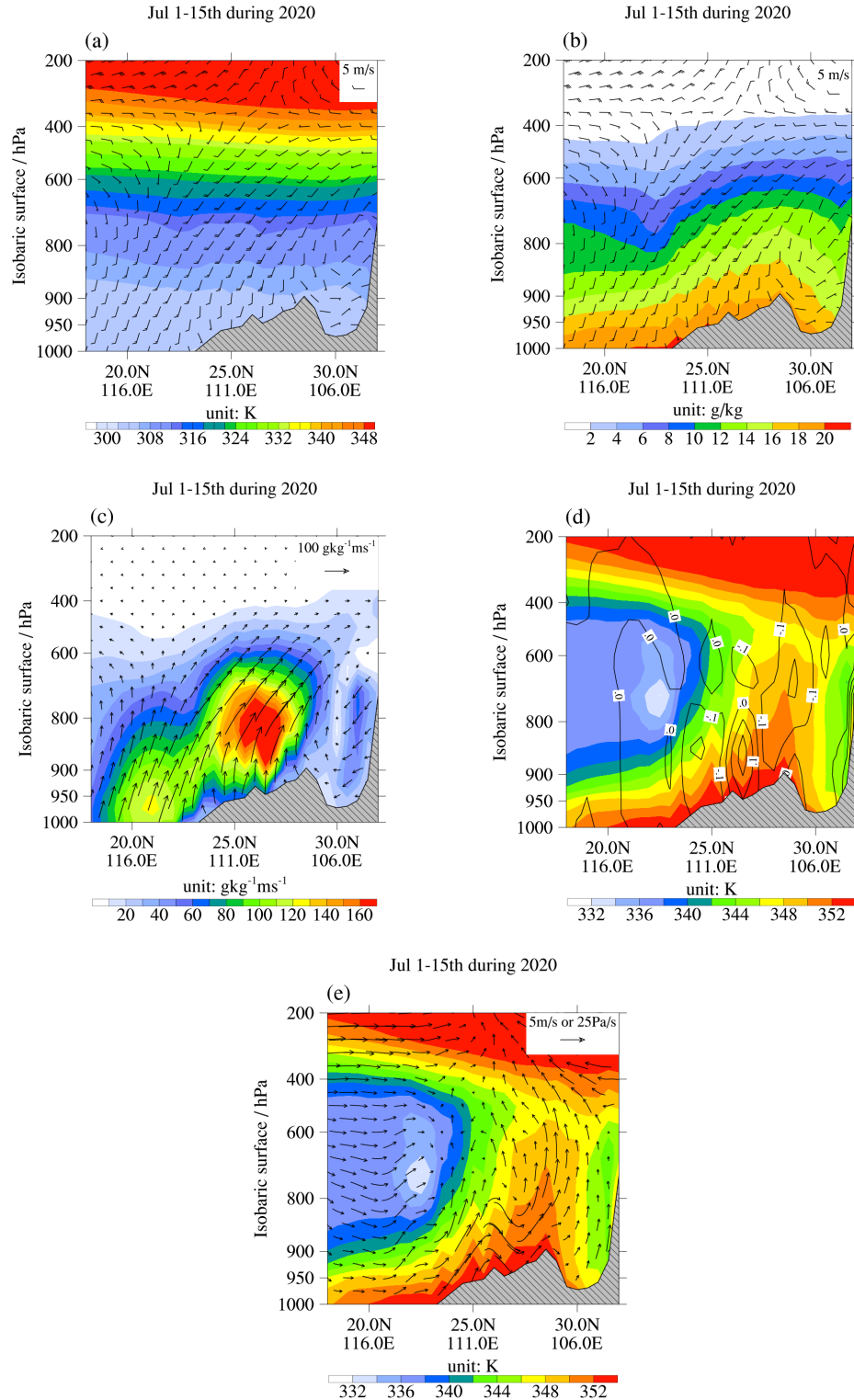


Figure 28. July 1-July 15. CFSR 15-days average cross-sections along ($18^{\circ}\text{N}, 118^{\circ}\text{E} - 32^{\circ}\text{N}, 104^{\circ}\text{E}$) for 2020. (a) Composite map of horizontal winds (m/s) and potential temperature (K). (b) Composite map of horizontal wind and specific humidity (g/kg). (c) Horizontal moisture flux ($\text{g} \cdot \text{kg}^{-1} \cdot \text{m} \cdot \text{s}^{-1}$). (d) Composite map of vertical velocity (pa/s) and equivalent potential temperature (K). (e) Composite map of atmospheric circulation and equivalent potential temperature (K). The grey shading area indicates terrain.

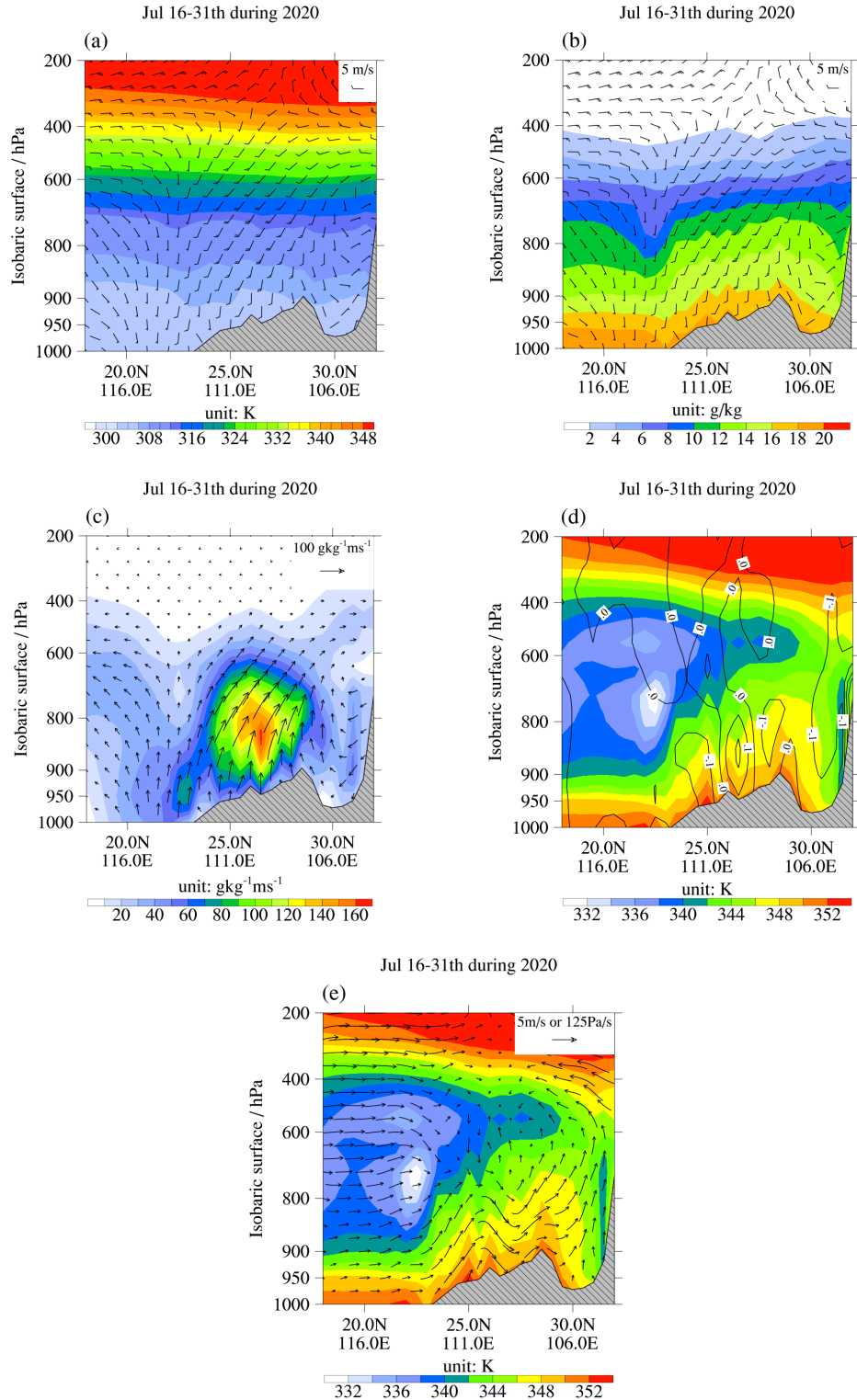


Figure 29. July 16-July 31. CFSR 15-days average cross-sections along ($18^{\circ}\text{N}, 118^{\circ}\text{E} - 32^{\circ}\text{N}, 104^{\circ}\text{E}$) for 2020. (a) Composite map of horizontal winds (m/s) and potential temperature (K). (b) Composite map of horizontal wind and specific humidity (g/kg). (c) Horizontal moisture flux ($\text{g} \cdot \text{kg}^{-1} \cdot \text{m} \cdot \text{s}^{-1}$). (d) Composite map of vertical velocity (pa/s) and equivalent potential temperature (K). (e) Composite map of atmospheric circulation and equivalent potential temperature (K). The grey shading area indicates terrain.

The vertical cross-section of equivalent potential temperature along the tilting axis (Figs. 21-28) can better depict the vertical structure of Mei-Yu frontal zone over the central China plain. In the prefrontal regions, the low-level air was warm and moist from the subtropical ocean whereas the air from the north comes from the polar region is relatively cold and dry. The clear difference between the shading area indicates the appreciable thermal and moist contrasts across the Mei-Yu front zone. During the 2020 Mei-Yu season, the moist air in the frontal region shows a moist tongue extending vertical upward corresponding well with the stronger frontal convection and heavy precipitation occurrences. It is apparent that the moist air is carried upward by the secondary circulation associated with the Mei-Yu jet/front system (Chen et al., 1994, 1997) (Figs. 21e-28e). In conclusion, the excessive rainfall during the 2020 Mei-Yu season is linked to the large moisture transport within the marine boundary layer by the stronger than normal MBLJ from the northern South China Sea. We also think that the moisture was carried upward in the frontal zone and the rainfall production is mainly related to the vertical motions associated with the Mei-Yu Jet/Front system (Figs. 25d, e-28d, e).

Over the Mei-Yu Jet/Front system, the southwesterly LLJ at a higher level (around 850-hPa) is largely related to the leeside low-pressure system (SWV) activities along the front. Previous studies by Chen et al. (1997) has proposed that the deepening of SWV along the Mei-Yu front shows some possible connections with the moist baroclinic process with large thermal gradient and latent heat release and an SLLJ along the front will be present under this circumstance. However, it is apparent that this southwesterly SLLJ in front of the SWV in the Mei-Yu frontal zone during the 2020 Mei-Yu season becomes much stronger than the ten-year mean conditions with higher wind speed. The reason why SLLJ along the front in 2020 is more vehement can be explained by the synergistic effects of SLLJ and MBLJ.

The MBLJ has been divided into two branches of tip jets due to the orographic blocking (Figs. 13b-16b) when arriving in the Hainan Island and then being lifted vertically to higher level (850-700-hPa) (Figs. 14 and 15, 25e-28e) over the frontal region because of the orographic lifting or secondary circulation associated with the Mei-Yu jet/front system (Chen et al., 1994,1997; Hsiao and Chen, 2014). Therefore, those low-level jets from the South China Sea were encountered with the strong south-westerly SLLJ in front of the SWV. The MBLJ merged with the Mei-Yu

jet/front system, providing moisture supply for the strong convection over Yangtze River Valley. As a result, the synergistic consists of SLLJ related to SWV and MBLJ contribute to the excessive heavy rainfall and flooding events during the 2020 Mei-Yu season.

By using the moist balance equation (Eq. (3)) (Yanai et al. 1973) given as below, we can better depict the moisture budget condition (Fig. 29) occurred over the Yangtze River Valley in terms of tendency (Term A, tendency term), horizontal moisture advection (Term B), vertical moisture convection (Term C) and subgrid-scale processes (Term D). We think that the moisture supply is mainly transported by the horizontal fluxes in the planetary layer from the northern South China Sea, however, the rainfall production is mainly related to the vertical motion associated with secondary circulation associated with the jet/front system.

$$\frac{\partial \bar{q}}{\partial t} = \underbrace{-\bar{V} \cdot \nabla \bar{q}}_A - \underbrace{\bar{\omega} \frac{\partial \bar{q}}{\partial p}}_B - \underbrace{[(\bar{c} - \bar{e}) + (\partial \bar{q}' \bar{\omega}' / \partial p)]}_C \quad (3) \quad \underbrace{\quad}_D$$

For the description of the cross-section along 110⁰E based on those 4 terms of moist balance equation during the entire prominent 2020 Mei-Yu season (Fig. 29), it is apparent that the tendency term (Term A) and horizontal advection term (Term B) are much smaller than vertical and subgrid-scale terms. It indicates that the heavy precipitation over the Yangtze River Valley during this early summer rainy season is mainly caused by the strong vertical motion. From the anomalies of vertical moisture transport along the tilting axis, it is evident that the anomalous horizontal vapor transport by the MBLJ brought in higher-than-normal moisture content to the frontal zone whereas the anomalous vertical motions and lifting in the frontal zone is the main reason for the production of excessive rainfall in the Yangtze River Valley.

The net precipitation (R) can be diagnosed from the moisture budget (Eq. (4)) in terms of net condensation rate “ \bar{c} ” and net evaporation rate “ \bar{e} ”, the moist budget equation was used to calculate the diagnosed rainfall and was compared with the rainfall data from the NCEP Reanalysis data results. After ignoring the surface evaporation, net surface precipitation rate (R) can be calculated by integrating the other terms of the moist budget equation within the troposphere (from 1000-hPa to 300-hPa).

$$\mathbf{R} = - \int_{P_B}^{P_T} (\bar{c} - \bar{e}) \frac{dp}{g} \quad (4)$$

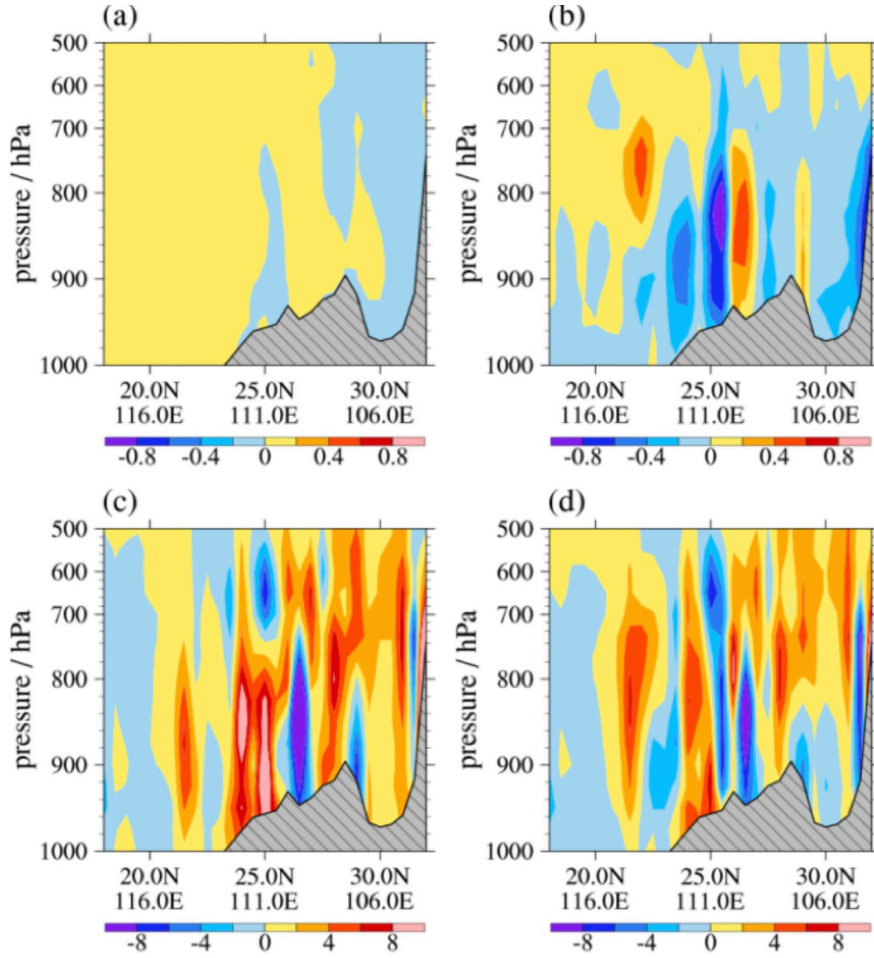


Figure 30. June 15 – July 31, 2020 CFSR average composite meridional cross-section along (18°N, 118°E – 32°N, 104°E) (a) The tendency term $(\partial \bar{q} / \partial t)$ ($10^{-5} \text{g} \cdot \text{kg}^{-1} \cdot \text{s}^{-1}$). (b) The horizontal Advection Term $(-V \cdot \nabla \bar{q})$ ($10^{-5} \text{g} \cdot \text{kg}^{-1} \cdot \text{s}^{-1}$). (c) The Vertical Advection Term $(-\bar{\omega} \frac{\partial \bar{q}}{\partial p})$ ($10^{-5} \text{g} \cdot \text{kg}^{-1} \cdot \text{s}^{-1}$). (d) Subgrid-scale Term $(-[(\bar{c} - \bar{e}) + (\partial \bar{q}' \omega' / \partial p)])$ ($10^{-5} \text{g} \cdot \text{kg}^{-1} \cdot \text{s}^{-1}$). The grey shading area indicates terrain.

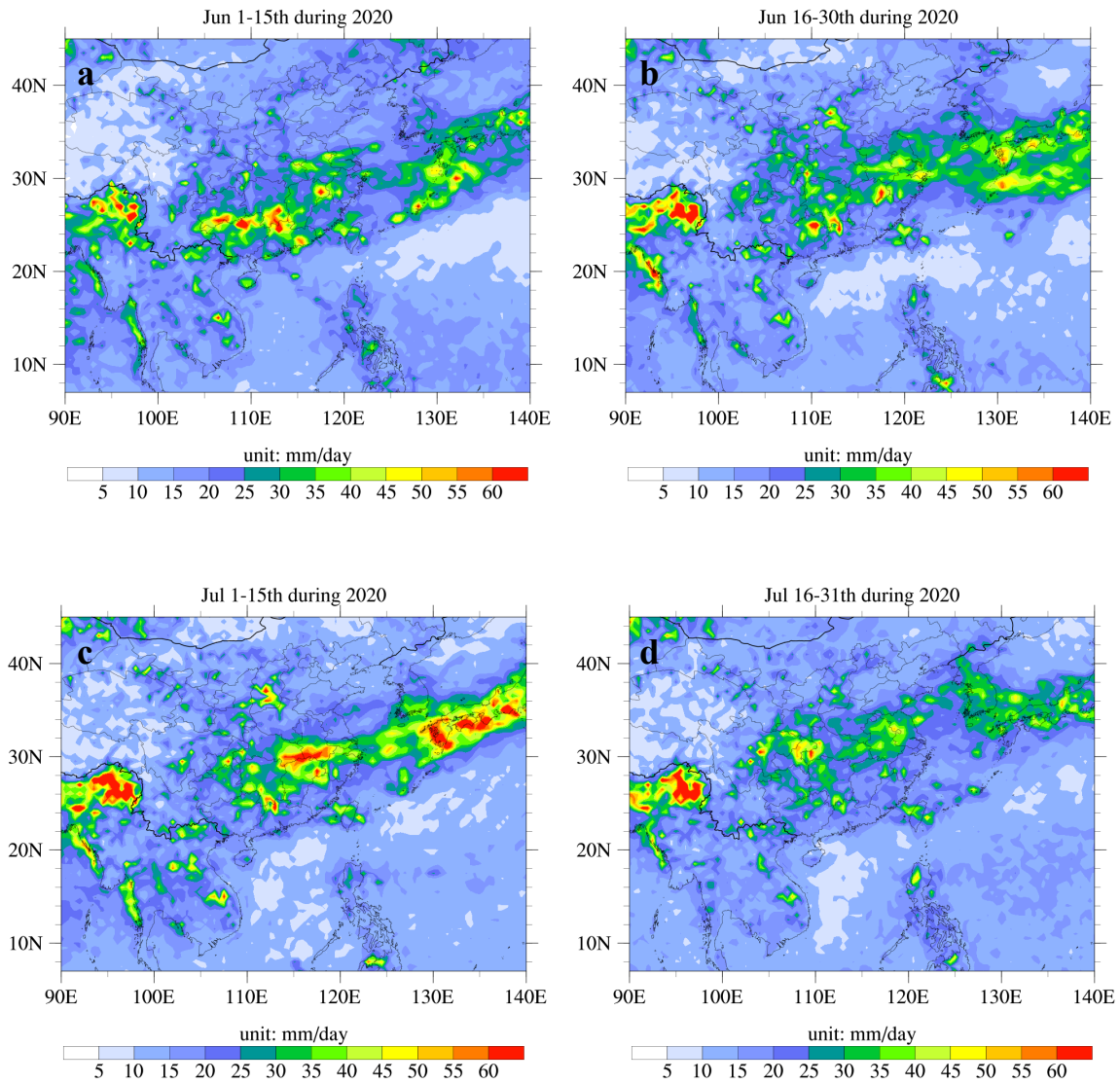


Figure 31. 2020 15-days Average Daily Precipitation Rate (mm/day) Rebuild Distribution (a)June 1 – June 15. (b)June 16 – June 30 (c)July 1– July 15. (d)July 16 – July 31.

The diagnosed daily precipitation rate distribution (Fig. 30) is in agreement with the precipitation distribution from the CFSR reanalysis data directly. The diagnosed precipitation pattern over the Bay of Bengal and Indian ocean area, fits well with CFSR reanalysis data. Over the southern China plain, Japan, and Korea where the precipitation is mainly from the Mei-Yu front the correspondence is also reasonable. In the future, it is desirable to investigate the possible reasons for discrepancies between the diagnosed rainfall patterns and reanalysis data.

4. Summary

During the 2020 early summer Mei-Yu rainy season in China, a series of unexpected heavy precipitation and flooding events occurred in the Yangtze River Valley, causing serious natural disasters, significant financial loss and casualties. Compared with the 15-days average synoptic ten-year mean conditions during the same time period in the past decade, the precipitation anomalies not only show its concentration in the middle and lower reaches of Yangtze River, but also illustrates its longer quasi-stationary Mei-Yu rainbands hovering around the central China plain. The average accumulated precipitation was 18% more than that in the same period of the year which is the second largest Mei-Yu precipitation since 1961.

Compared with the synoptic low-level conditions at the same time in the past nine years (2011 – 2019 annual mean) (Fig. 2,3,4,5), the low-level synoptic field during the 2020 Mei-Yu season (June 1st -July 31st) shows the existence of stronger West Pacific Subtropical High (WPSH) and a deeper South-West Vortex with warmer potential temperature. Even though the ridge of WPSH shows a relatively steady position in the meridional direction, the WPSH extended westward than climatological mean (Fig. 2b,3b,4b,5b), penetrating into the Southern China Plain with relatively warmer and dryer conditions over the southern China coastal and Taiwan areas. Under the normal conditions, May and early June are the Mei-Yu season for the southern China coastal area and Taiwan, which is about one month earlier than the Mei-Yu season over Southern China Plain (Fig. 2a). However, due to the westward extension of WPSH, Taiwan and Southern China coastal areas suffered warmer and drier air during this particular time with relatively lower precipitation than usual (Fig. 1 and 2).

The characteristics of synoptic patterns during the 2020 early summer rainy season over the East Asia may illustrate this unusual Mei-Yu precipitation in multiple ways. Even though during the Mei-Yu season over the past years, the semi-permanent subtropical high pressure over the west Pacific (WPSH) extended westward (113°E) and strengthened when compared with the ten-year mean. The intensity of WPSH during the 2020 Mei-Yu season shows positive anomalies ($> 36 \text{ gpm}$) accompanied by westward and northward extension. In the mid-troposphere (500-hPa), the variation of the East Asian trough (110°E - 120°E) also corresponds well with the WPSH, having

positive anomaly (> 36 gpm) and shifted westward. As for the mid and -upper-level circulation patterns, the weakening of the Bengal Depression over the Indian Ocean corresponds well with the strengthening of the upper-level westerly wind over the Tibetan Plateau which may result in deepening and warmer SWV. In addition, the low-level synoptic patterns depict that the cold air masses invading from the polar region with temperatures cooler than the ten-year mean, contributing to the strong thermal wind and baroclinity along the Mei-Yu front.

The MBLJ is mainly due to the pressure gradients between the WPSH and of a southwest vortex which formed on the lee side of Tibetan Plateau and then moves eastward (Tu et al. 2019). During the 2020 Mei-Yu season, the low-level atmospheric circulation over the South China Sea shows a large meridional wind component due compared to the ten-year mean due to the existence of a stronger than ever WPSH. During the entire 2020 Mei-Yu season the MBLJ over the northern South China Sea south of the Hainan Island is a prominent feature. With its direction pointing to the southern China plain directly, this MBLJ shows its importance in transporting moisture from the northern South China Sea to the southern China. The abnormal synoptic patterns caused a relatively large pressure gradients between SWV and the westward shifting and strengthening of WPSH, contribute to the strength and direction of the MBLJ.

From the meridional cross-section of MBLJ, it indicates that the MBLJ plays any important role in low-level moisture transport from the northern South China Sea to the Yangtze River Valley during the 2020 Mei-Yu season. The unusual MBLJ from the South China Sea encountered with the southwesterly SLLJ ahead of the SWV along the front with abundant moisture supply inside. From the moist budget balance (Figs. 25-28), it is evident that the rainfall is caused by the secondary circulation associated with the jet/front system over the Yangtze River Valley whereas anomalous moisture transport by the MBLJ provides the excessive moisture sources for the unusual heavy precipitation occurred over the Yangtze River Basin. Under this condition, the synergistic effect made by MBLJ and SLLJ, finally causes the extremely strong and moist LLJ together ($> 10 \text{ ms}^{-1}$) ($> 160 \text{ g} \cdot \text{kg}^{-1} \cdot \text{ms}^{-1}$) along the Mei-Yu. Moreover, the moisture transport is dominated by the mean flow with much less contribution by the transient mode resulted in the frequent heavy rainfall periods during the 2020 Mei-Yu Season.

As for our next step, we will look into the reason that causes the unusual strength and westward extension of. We also intend to test our hypothesis of the impacts of MBLJ on extremely Mei-Yu precipitation by using the WRF-ARW 9-km model output. By using the same researching approach in this article, we also want to analyze the Mei-Yu season in 1961 when there are similar unprecedented rainfall events occurred over the Yangtze River Valley.

APPENDIX

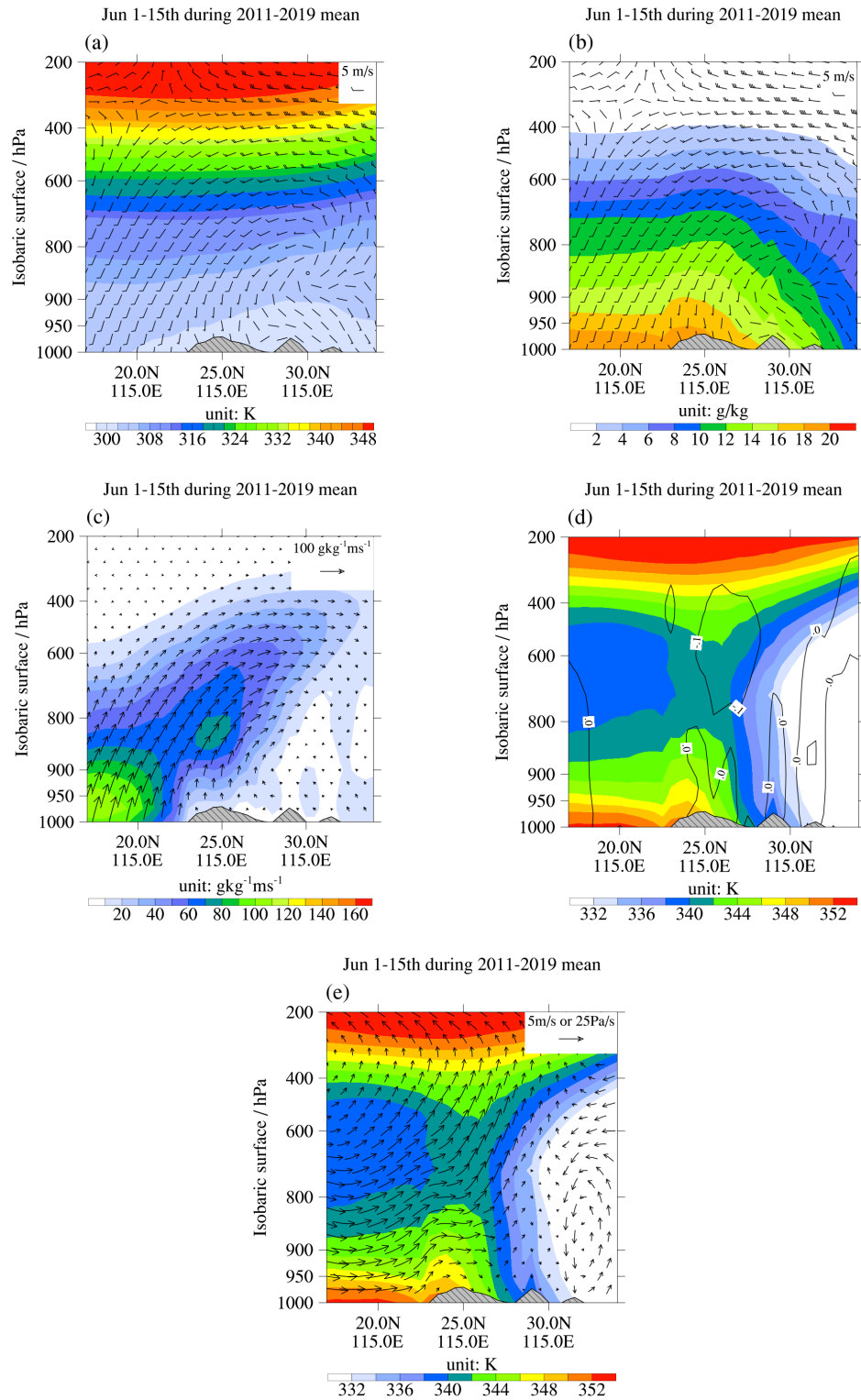


Figure 32. As in Fig.22 but for meridional cross-section along (18°N, 118°E – 32°N, 104°E).

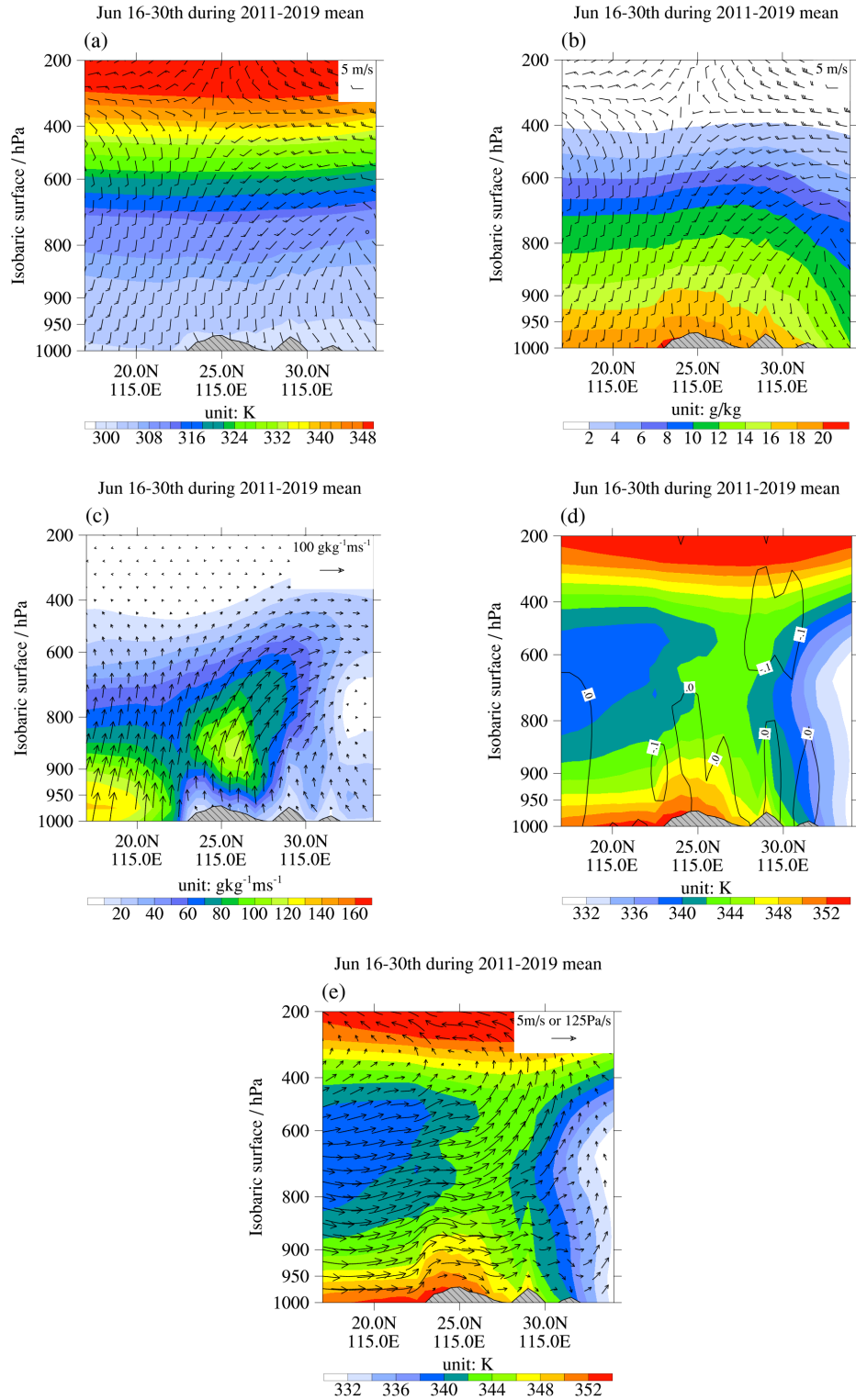


Figure 33. As in Fig.23 but for meridional cross-section along ($18^{\circ}\text{N}, 118^{\circ}\text{E} - 32^{\circ}\text{N}, 104^{\circ}\text{E}$).

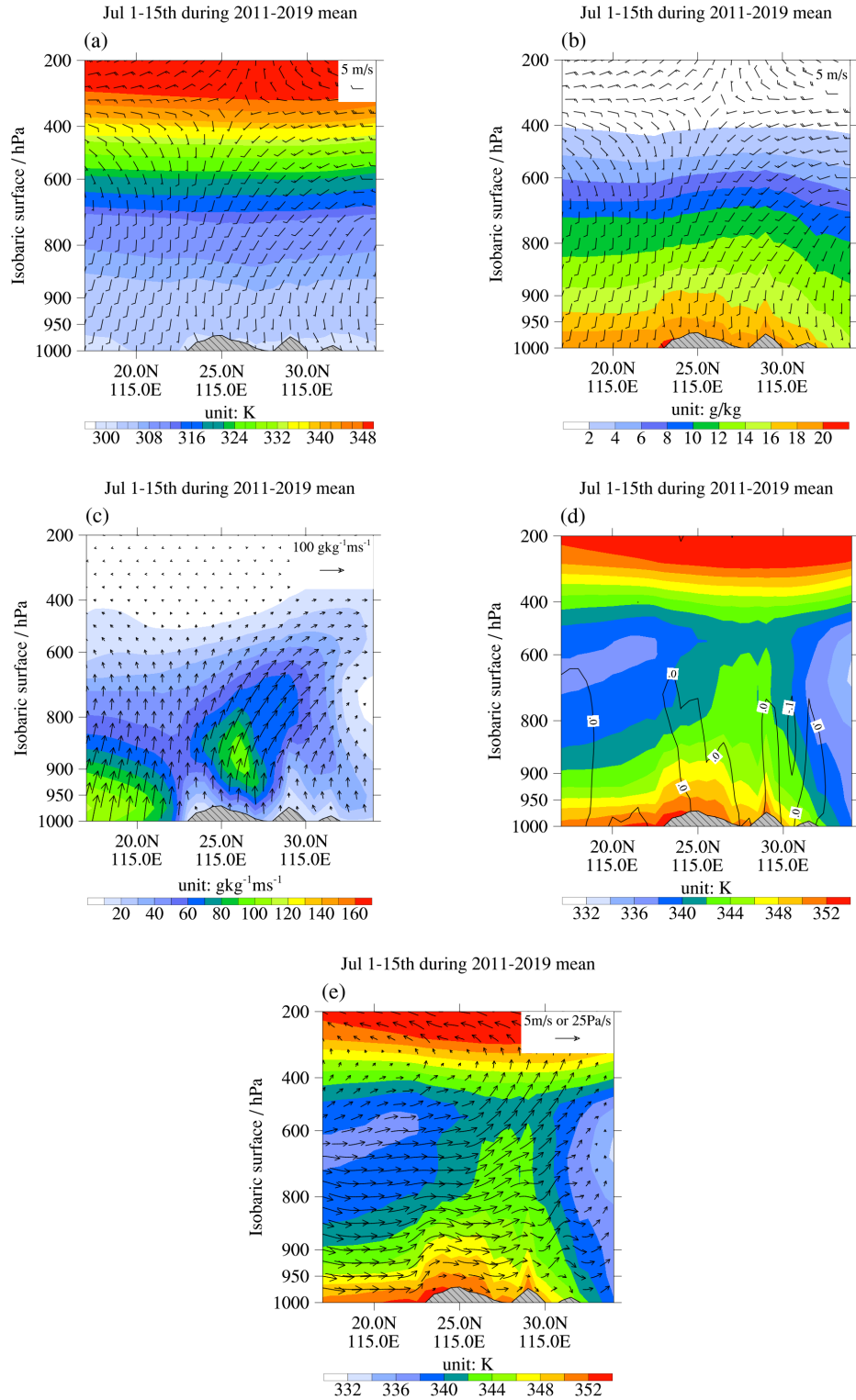


Figure 34. As in Fig.24 but for meridional cross-section along (18°N, 118°E – 32°N, 104°E).

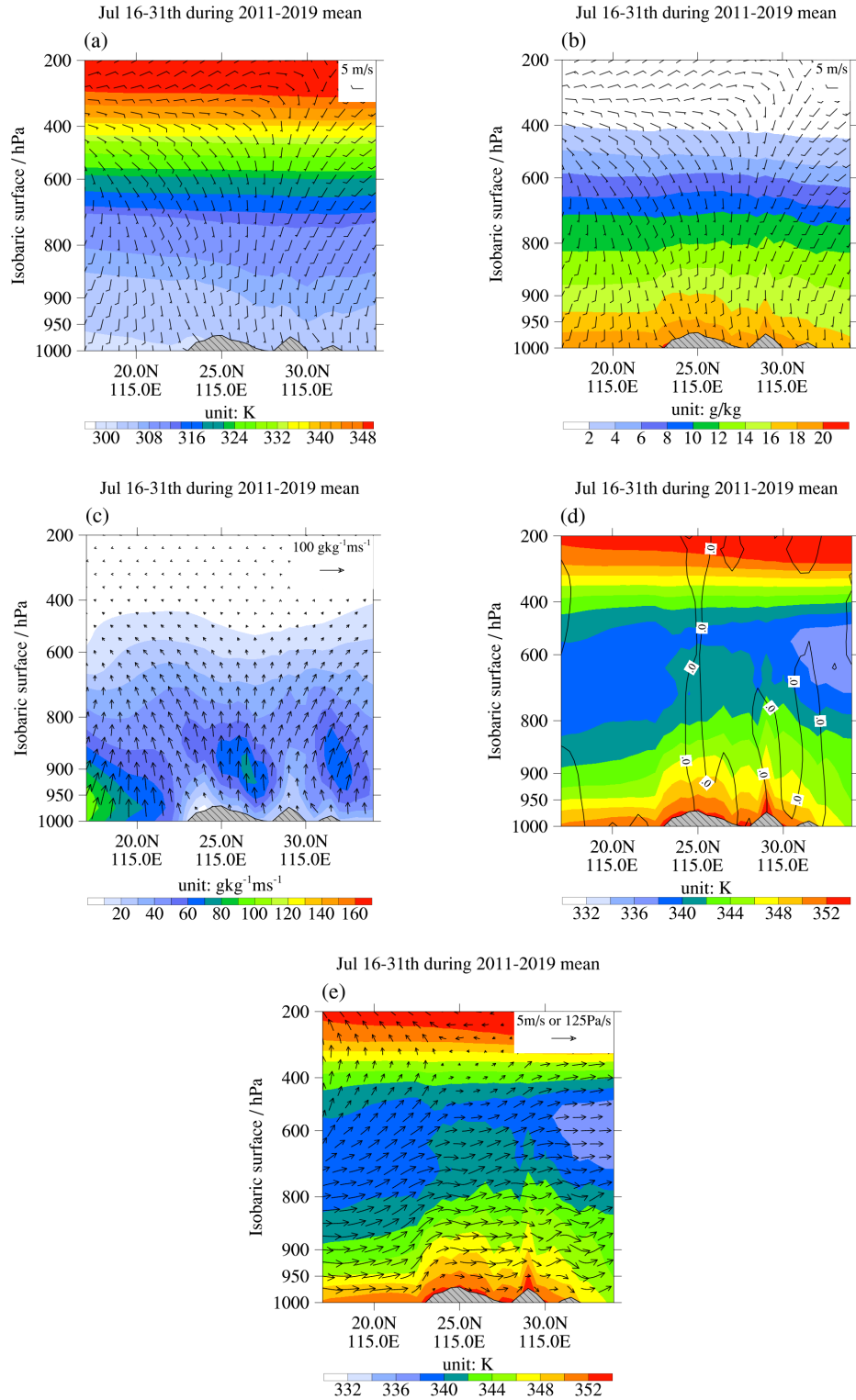


Figure 35. As in Fig.25 but for meridional cross-section along (18°N, 118°E – 32°N, 104°E).

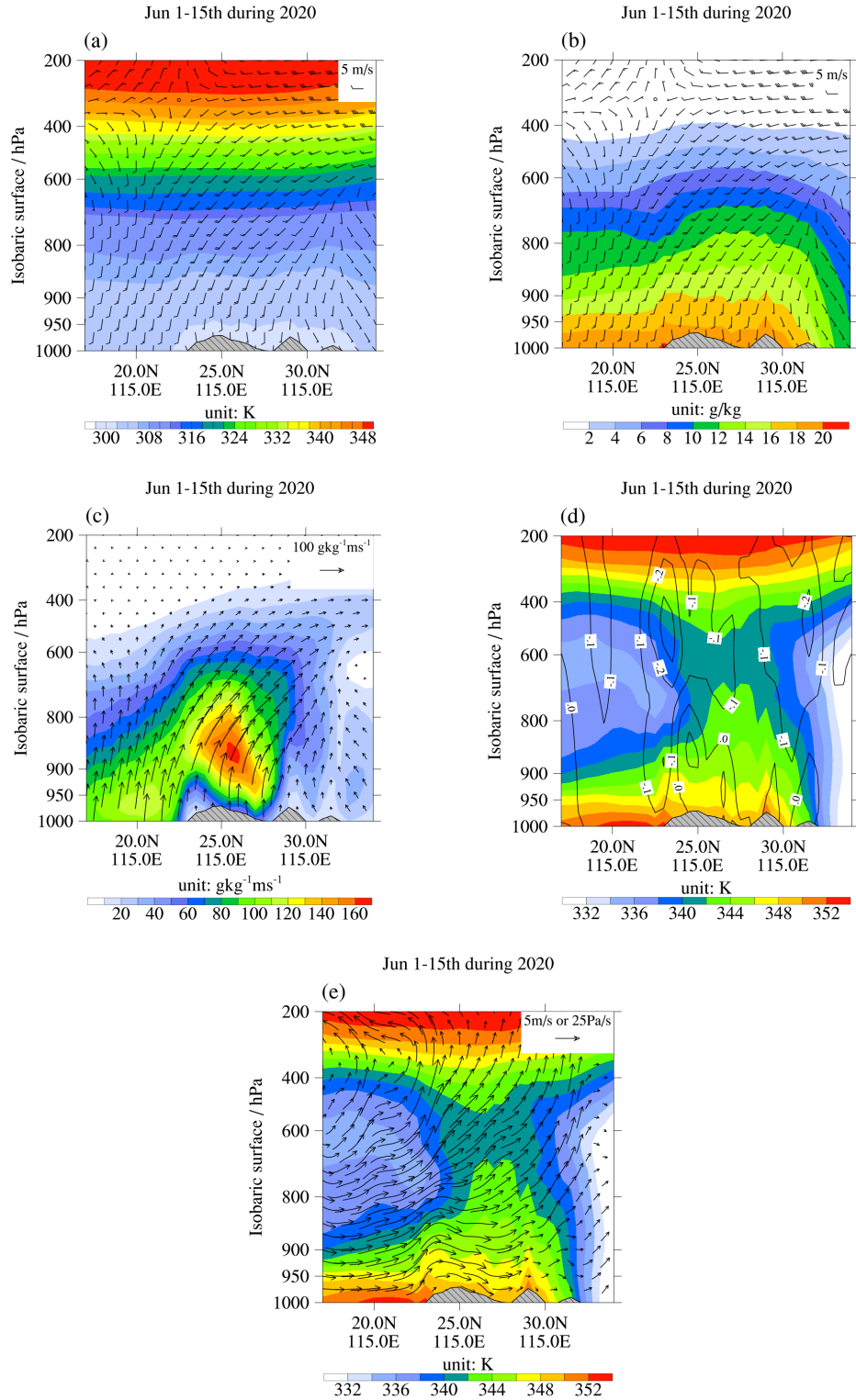


Figure 36. As in Fig.26 but for meridional cross-section along (18°N, 118°E – 32°N, 104°E).

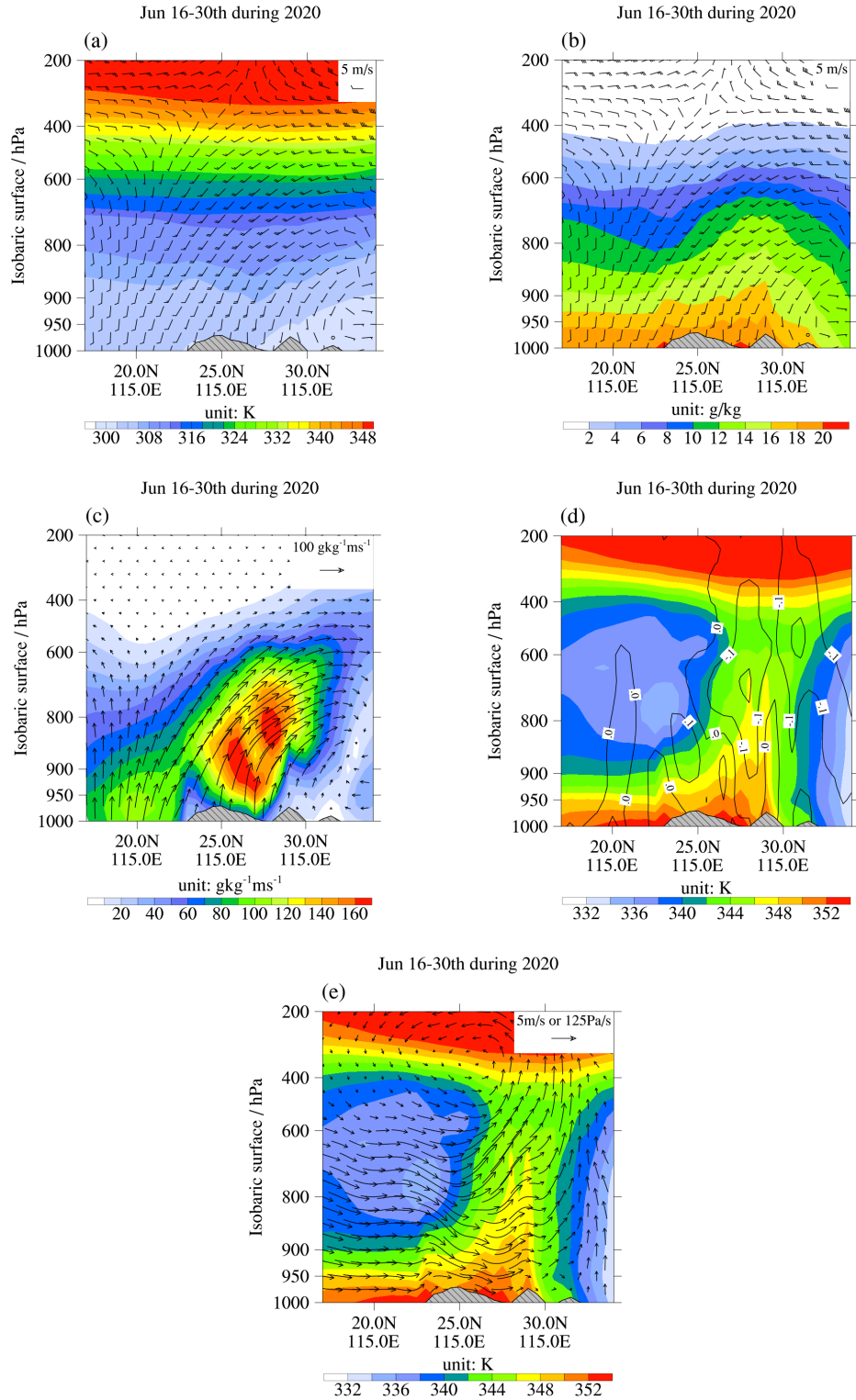


Figure 37. As in Fig.27 but for meridional cross-section along (18°N, 118°E – 32°N, 104°E).

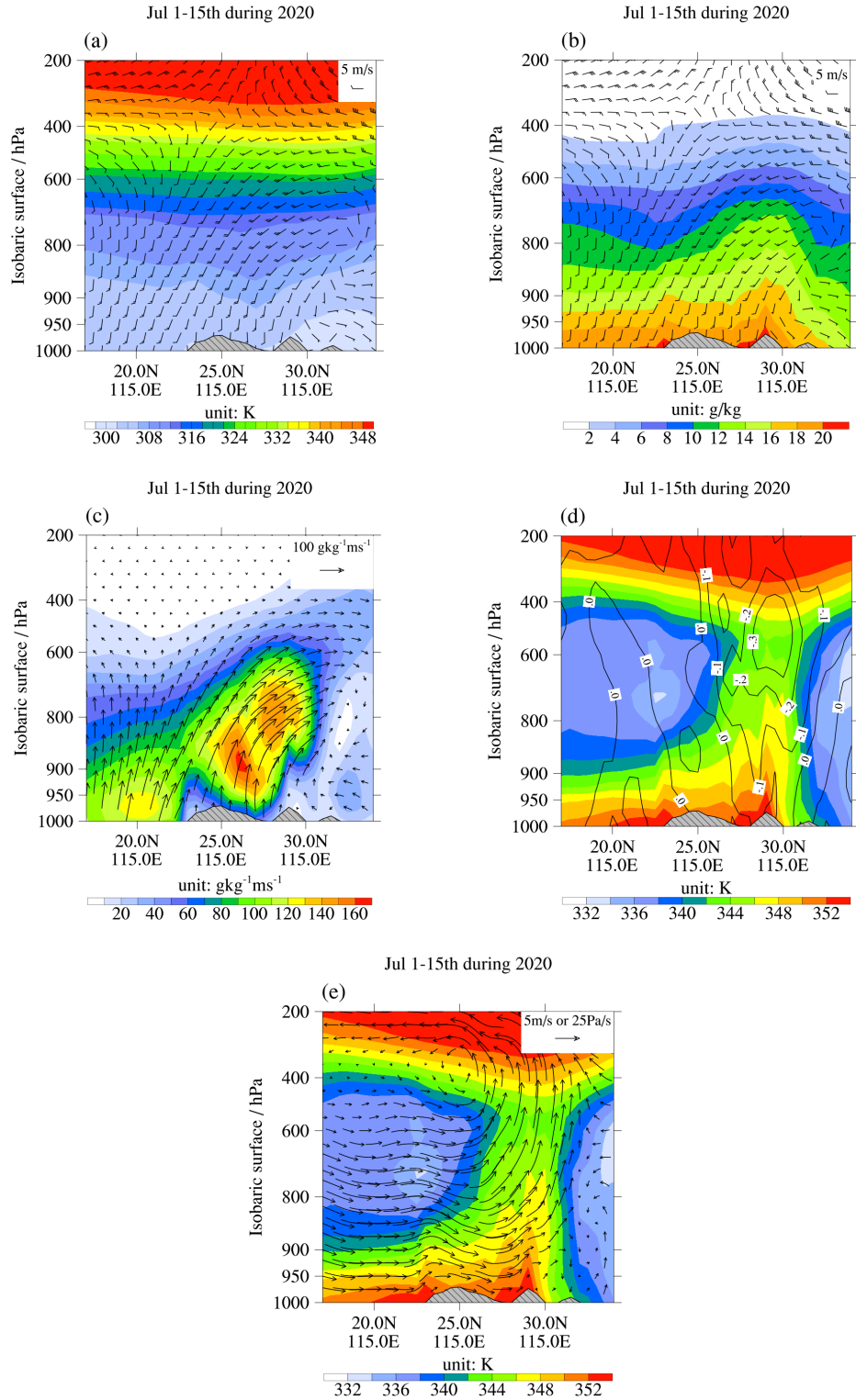


Figure 38. As in Fig.28 but for meridional cross-section along ($18^{\circ}\text{N}, 118^{\circ}\text{E} - 32^{\circ}\text{N}, 104^{\circ}\text{E}$).

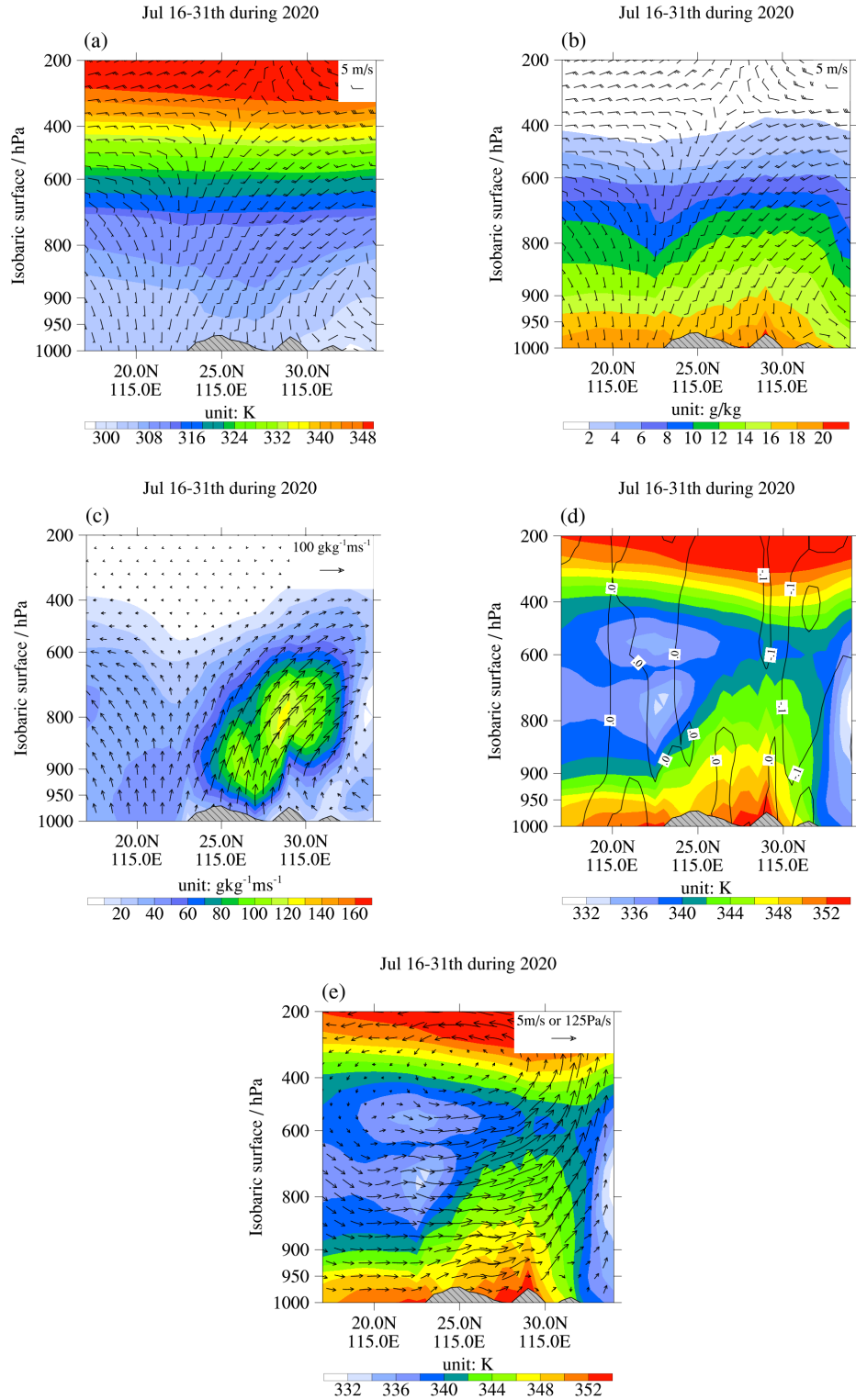


Figure 39. As in Fig.22 but for meridional cross-section along (18°N, 118°E – 32°N, 104°E).

References

- [1] Chen Y L, Chen X A, Zhang Y X. A Diagnostic Study of the Low-Level Jet during TAMEX IOP 5[J]. *Monthly Weather Review*, 1995, 122(10):2257-2284.
- [2] Chen, Y.-J. Chu, C.-S. Chen, C.-C. Tu, J.-H. Teng, and P.-L. Lin, 2018: Analysis and simulations of a heavy rainfall event over northern Taiwan during 11–12 June 2012. *Mon. Wea. Rev.*, 146, 2697–2715, <https://doi.org/10.1175/MWR-D-18-0001.1>.
- [3] Tu, C., Y. Chen, P. Lin, and Y. Du, 2019: Characteristics of the Marine Boundary Layer Jet over the South China Sea during the Early Summer Rainy Season of Taiwan. *Mon. Wea. Rev.*, 147, 457–475, <https://doi.org/10.1175/MWR-D-18-0230.1>.
- [4] Chen, G. T.-J., and C.-C. Yu, 1988: Study of low-level jet and extremely heavy rainfall over northern Taiwan in the mei-yu season. *Mon. Wea. Rev.*, 116, 884–891, [https://doi.org/10.1175/1520-0493\(1988\)116,0884:SOLLJA.2.0.CO;2](https://doi.org/10.1175/1520-0493(1988)116,0884:SOLLJA.2.0.CO;2).
- [5] Chen, Y.-L., 1993: Some synoptic-scale aspects of the surface fronts over southern China during TAMEX. *Mon. Wea. Rev.*, 121, 50-64.
- [6] Chen, Y.-L., 1989: Aspects of midlatitude influences on the surface front over southern China during TAMEX. *Papers. Meteor. Res.*, 12, 159-174.
- [7] Chen, X. A., and Y.-L. Chen, 1995: Development of low-level jets during TAMEX. *Mon. Wea. Rev.*, 123, 1695–1719, [https://doi.org/10.1175/1520-0493\(1995\)123,1695:DOLLJD.2.0.CO;2](https://doi.org/10.1175/1520-0493(1995)123,1695:DOLLJD.2.0.CO;2).
- [8] Yanai, M., S. Esbensen, and J.-H. Chu, 1973: Determination of bulk properties of tropical cloud clusters from large-scale heat and moisture budgets. *J. Atmos. Sci.*, 30, 611–627, [https://doi.org/10.1175/1520-0469\(1973\)030,0611:DOBPOT.2.0.CO;2](https://doi.org/10.1175/1520-0469(1973)030,0611:DOBPOT.2.0.CO;2).
- [9] Ogura, Y., and H. Cho, 1973: Diagnostic Determination of Cumulus Cloud Populations from Observed Large-Scale Variables. *J. Atmos. Sci.*, 30, 1276–1286, [https://doi.org/10.1175/1520-0469\(1973\)030<1276:DDOCCP>2.0.CO;2](https://doi.org/10.1175/1520-0469(1973)030<1276:DDOCCP>2.0.CO;2).
- [10] Wang, B., R. Wu, and X. Fu, 2000: Pacific–East Asian Teleconnection: How Does ENSO Affect East Asian Climate?. *J. Climate*, 13, 1517–1536, [https://doi.org/10.1175/1520-0442\(2000\)013<1517:PEATHD>2.0.CO;2](https://doi.org/10.1175/1520-0442(2000)013<1517:PEATHD>2.0.CO;2).

[11] Hsiao, F., and Y.-L. Chen, 2014: Revisiting the structure and characteristics of an early summer monsoon trough over South China in 1975. SOLA, 10, 194–198, <https://doi.org/10.2151/sola.2014-041>.

[12] MJO Monthly Report prepared by the Climate Prediction Center (NCEP), <https://www.cpc.ncep.noaa.gov/products/precip/CWlink/MJO/ARCHIVE/PPT/>

[13] Tu, Chuan-Chi & Chen, Yi-Leng & Lin, Pay-Liam & Lin, Po-Hsiung. (2020). The relationship between the boundary layer moisture transport from the South China Sea and heavy rainfall over Taiwan. *Terrestrial Atmospheric and Oceanic Sciences*. 31. 159-176. 10.3319/TAO.2019.07.01.01.